

Magnetic Resonance Spectroscopy (MRS) and Its Application in Alzheimer's Disease

PRAVAT K. MANDAL^{1,2,3}

¹Department of Psychiatry, Western Psychiatric Institute and Clinic, University of Pittsburgh Medical School, Pittsburgh, Pennsylvania

²Center for Neuroscience, University of Pittsburgh Medical School, Pittsburgh, Pennsylvania

³Department of Bioengineering, University of Pittsburgh, Pittsburgh, Pennsylvania

ABSTRACT: Magnetic resonance spectroscopy (MRS) is a noninvasive tool to measure the chemical composition of tissues (in vivo) and characterize functional metabolic processes in different parts of the human organs. It provides vital biological information at the molecular level. Combined with magnetic resonance imaging (MRI), an integrated MRI/MRS examination provides anatomical structure, pathological function, and biochemical information about a living system. MRS provides a link between the biochemical alterations and the pathophysiology of disease. This article provides a comprehensive description of the MRS technique and its application in Alzheimer's disease (AD) research. This review is a primer for students and researchers seeking a firm theoretical understanding of MRS physics as well as its application in clinical AD research. © 2007 Wiley Periodicals, Inc. Concepts Magn Reson Part A 30A: 40–64, 2007

KEY WORDS: MRS; MRI; PRESS; STEAM; 2D MRS; Alzheimer's disease

I. INTRODUCTION

Magnetic resonance spectroscopy (MRS) is a rapidly developing field of neuroimaging that allows noninvasive in vivo analysis of metabolites. It

selectively excites a small volume of tissue (voxel) using gradients, then records the free induction decay (FID) and produces a spectrum from the FID originating from that voxel. In the 1980s the first MR spectrum from living brain was published, and studies were performed on patients with stroke or brain tumors (1–3). Over the past two decades, MRS has been performed on patients with a wide range of neurological and psychiatric disorders so as to increase the understanding of the pathological mechanisms of these disorders. MRS is also applied to monitor long-term changes with or without drug therapy and to identify differences between diagnostic groups.

Received 1 August 2006; revised 12 October 2006; accepted 12 October 2006

Correspondence to: Dr. Pravat K. Mandal; E-mail: mandalp@upmc.edu

Concepts in Magnetic Resonance Part A, Vol. 30A(1) 40–64 (2007)

Published online in Wiley InterScience (www.interscience.wiley.com). DOI 10.1002/cmra.20072

© 2007 Wiley Periodicals, Inc.

Table 1 Nuclei Used for MRS In Vivo

Nucleus	Name	Spin Number	Frequency ν at $B_0 = 1.5$ Tesla	Inherent Sensitivity at Const. Field ($^1\text{H} = 1$)	Natural Abundance (%)
^1H	Hydrogen (protons)	$\frac{1}{2}$	63.87	1	99.985
^{13}C	Carbon	$\frac{1}{2}$	16.06	0.0159	1.108
^{19}F	Fluorine	$\frac{1}{2}$	60.08	0.833	100
^{23}Na	Sodium	$\frac{3}{2}$	16.89	0.0925	100
^{31}P	Phosphorus	$\frac{1}{2}$	25.85	0.0663	100
^{35}Cl	Chlorine	$\frac{3}{2}$	6.26	0.0047	75.53
^{39}K	Potassium	$\frac{3}{2}$	2.98	0.00051	93.08

MRS is a nondestructive technique, which does not require any ionizing radiation. It provides a wealth of information (in vivo) on various neurometabolites from a single experiment. It does not require metabolite isolation or sample treatment, as required by mass spectrometry or other analytical methods. In recent years, there have been a number of technical advances concerning both the implementation of different MRS pulse sequences, data processing, and commercial availability of more sophisticated high-field scanners.

MRS techniques have been developed and applied extensively in brain research (4). The brain has multiple levels of compartmentation ranging from the type of cellular compartment (neuron versus astrocyte) to the type of tissue compartment (the gray matter vs. the white matter) to distinct central nervous systems and brain functions. These compartments are highly integrated and work together to attain various brain functions. MRS is useful in understanding the neurochemical changes in the brain due to different physiological processes. The extensive numbers of MRS applications have been reported exclusively in the brain due to the lack of motion artifacts in the brain. In addition, the brain is more or less spherical; hence, it is easier to adjust the high degree of homogeneous magnetic field by shimming for MRS studies. However, there are susceptibility differences in the brain between the intracellular and extracellular space.

The unique applications of MRS in brain research are (1) quantification of oxidative state of the brain and defining neuronal death; (2) accessing and mapping neuronal damage; (3) evaluating membrane alteration and characterizing encephalopathies (disturbances in brain functioning, particularly in intellectual activity or higher cortical functioning). MR spectroscopy enables detection of abnormalities in several neurodegenerative diseases, such as Alzheimer's disease (AD), and plays an important role in research studies of dementia (5, 6). However, despite these advances, there is still a large gap between the MRS techniques development and the challenge of

implementing them in a hospital environment for diagnostic purposes (7, 8).

The Basics of MRS

The fundamental basis of MRS is governed by the same principles of nuclear magnetic resonance (NMR) (9–21). MRS requires a magnetic field and a radio frequency (RF) transmit pulse at a particular resonant frequency to observe the signal of a specific nuclei (e.g., ^1H , ^{31}P , ^{13}C etc.) in the region of interest (Table 1). The product of MRS is a “spectrum” with a frequency axis in parts per million (ppm) and a signal amplitude axis (22–28). The signal amplitude (area) is a measure of a particular metabolite concentration. Specific nuclei (e.g., ^1H , ^{31}P , ^{13}C , and so on) from the metabolite, depending on their characteristic signature, give rise to either a single peak or multiple peaks that are uniquely positioned along the frequency axis (X axis), known as the chemical shift. The dispersion of chemical shift (along the X axis) increases with magnetic field strength. The peak amplitude (area) that is directly related to the concentration of that assigned metabolite is displaced along the Y axis. In vivo ^1H -MRS and ^{31}P -MRS are the most widely used applications of MRS, but other atoms that are used for MRS studies include ^{13}C , ^{15}N , ^{19}F , and ^{23}Na . Major metabolites detected by ^1H MRS are as follows:

- N-acetyl aspartate (NAA) is a neuronal marker seen only in nervous tissue.
- Glutamate (Glu) and glutamine (Gln) complex is a mixture of peaks that helps to monitor glutamate metabolism in the brain for chronic epileptic activities.
- Lactate is a highly specific marker of cell death as well as tissue necrosis.
- Creatine (Cr) is thought to be a marker of energetic status of cells.
- Choline (Cho), an indicator of membrane activity, is often elevated in the presence of malignant processes.

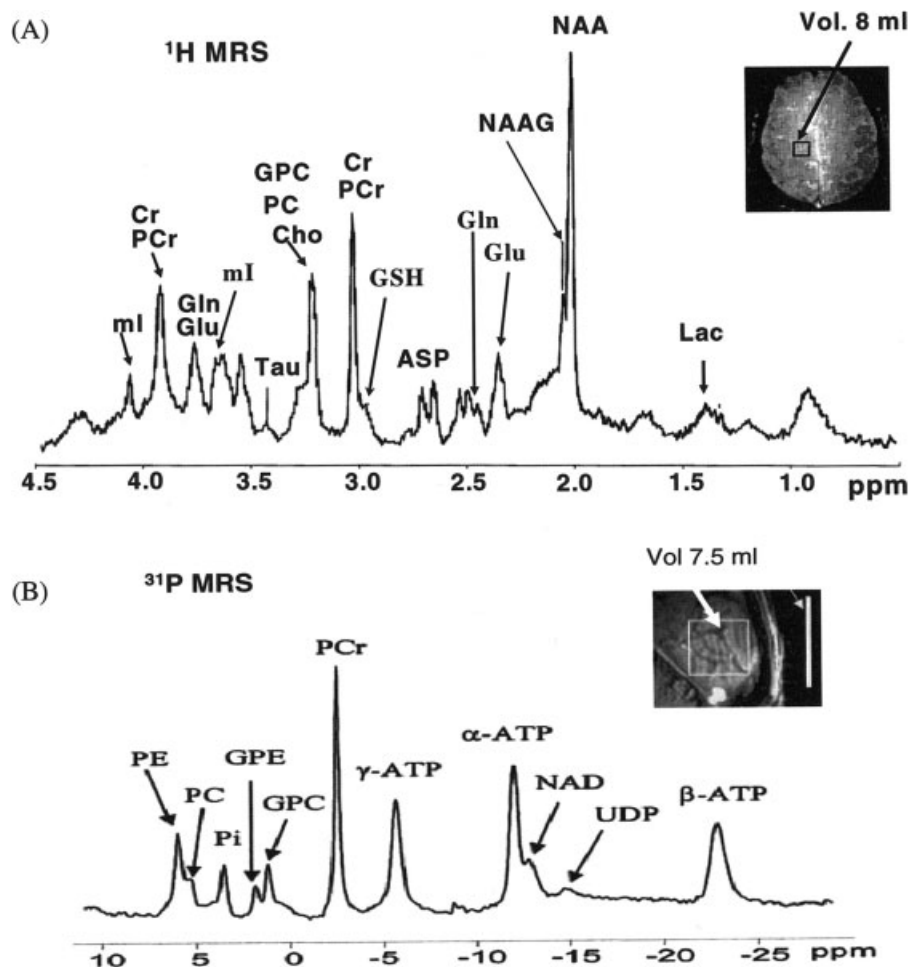


Figure 1 (A) ^1H MRS spectrum (97) and (B) ^{31}P MR spectrum (32) from parietal white matter at 7 T in normal human brain using STEAM pulse sequence. Inset indicates voxel location.

- *Myo-inositol* (*mI*), a sugar alcohol, is a marker of astrocytic activity and is often higher in conditions such as AD and malignant tumors.

In recent years, there has been more interest in ^1H MRS, particularly after it was demonstrated that it was possible to obtain high-resolution spectra from small, well-defined regions in reasonably short scan times. The higher sensitivity of the proton is due to several factors, including higher gyromagnetic ratio, higher metabolite concentrations, and favorable ^1H relaxation times. Although the sensitivity of ^{31}P MRS is less than ^1H MRS, ^{31}P MRS provides insights into the biochemistry not available by ^1H MRS (29, 30). ^{31}P MRS detects high-energy metabolites: adenosine triphosphate (ATP), phosphocreatine (PCr), and inorganic phosphate (Pi). ^{31}P MRS allows noninvasive assessment of various fundamental biochemical, physiological, and energy intensive metabolic events occurring inside the brain (31, 32). The steady-state phosphate signals as

well as other physiological parameters detected by *in vivo* ^{31}P MRS have been used extensively in clinical studies and linked to numerous diseases such as AD (33), epilepsy (34, 35), migraine, brain ischemia, and seizure (36). Figure 1 represents a typical ^1H and ^{31}P MRS spectrum of the brain at 7 T magnetic field.

To enhance the signal-to-noise ratio (SNR) of the MR spectrum, the pulse sequence and the parameters are adjusted to minimize signal intensity loss due to T_2 (transverse) and T_1 (longitudinal) relaxation of the nuclei (e.g., ^1H , ^{31}P , and ^{13}C). As mentioned previously, the MRS technique is applied in conjunction with MRI, and both techniques share similarities and differences as outlined below.

Similarities with MRI

- The same scanner is used for both MRI and MRS studies. A schematic diagram of a scanner is shown in Fig. 2.

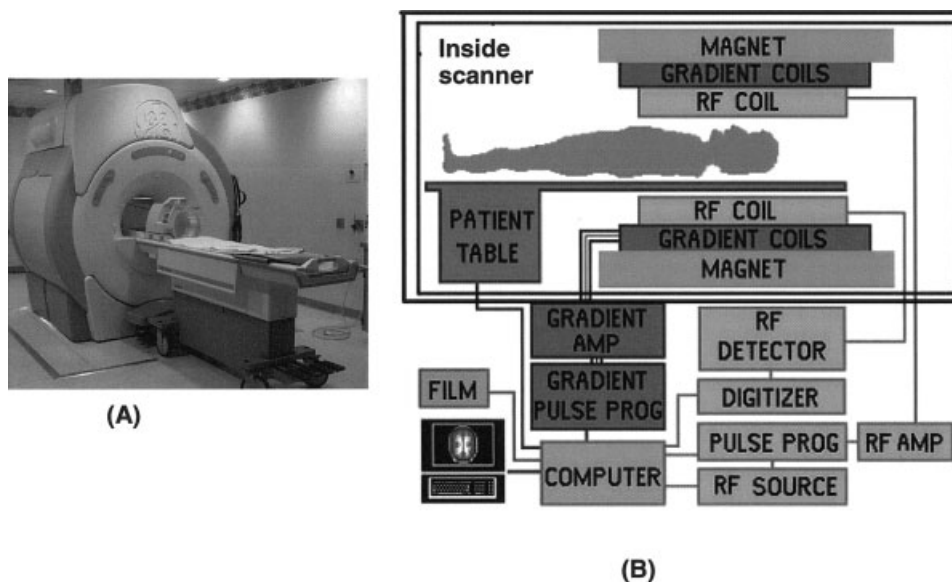


Figure 2 (A) Scanner. (B) The components of a scanner used for MRS and MRI studies.

- Both techniques are based on the same physical principles (i.e., the detection of energy exchange between external magnetic fields and specific nuclei within the tissue).
- Both techniques use a magnetic field instead of radiation. Generally, the patient is placed supine (face up) inside the scanner. A special RF coil is placed around the patient's head and MRI/MRS experiments are performed.
- Both techniques extensively use gradients for spatial localization and dephasing the unwanted magnetization.
- MRI and multiple-voxel MRS experiments both use phase-encoding gradients (Fig. 3).

Differences with MRI

- In MRI, the magnetic field is used to create images based on proton signals from water content among tissues and organs. MRI images contain anatomical information based on the distribution of protons (from water) as well as the relative proton relaxation rates in various tissues.
- In MRS, magnetic field is used for creating a graph. This graph consists of various peaks, each of which represents a specific metabolite in the specific region of interest. The presence or absence, as well as increase or decrease in peak area, provide insight into various neurochemical processes occurring in the tissue.
- MRS is generally less sensitive than MRI because the concentrations of nuclei (^1H , ^{31}P , and so on from the neurometabolites) as measured by MRS

- are orders of magnitude less concentrated compared to the concentration of hydrogen (from water) generally involved in MRI.
- MRI provides information on the physical-chemical state of tissues, flow diffusion, and motion. MRS provides chemical composition of tissues from the particular region of interest.

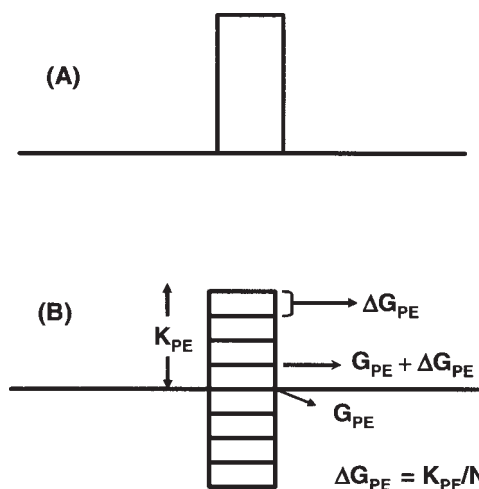


Figure 3 (A) Normal magnetic field gradient and (B) phase-coding magnetic field gradients that allow the encoding of the spatial signal location along a second dimension by different spin phases. Amplitude is kept fixed in a normal magnetic field gradient. In phase-encoding gradient, amplitude is typically varied from a minimum value of $-K_{PE}$ to maximum value of $+K_{PE}$ in N steps, where K_{PE} refers to the amplitude of the phase-encoding gradient. The spatial resolution is directly related to the number of phase-encoding steps.

- Common uses of MRI include the detection of AD, stroke versus tumor, recurrent or residual tumor following therapy versus successfully treated tumor, infection or abscess, and many others. MRS does not diagnose a given condition, but rather provides additional data to aid in diagnosis, and it must be interpreted along with clinical history and other imaging studies, such as MRI.
- In MRI, readout gradient (frequency encoding) is turned on during data acquisition time. In MRS, no frequency-encoding gradients are necessary during data collection due to inherent chemical shift difference of the nuclei (e.g., ^1H , ^{31}P , ^{13}C , etc.) in a given tissue volume.
- In a single-voxel MRS experiment there is no application of phase-encoding gradient, whereas phase encoding gradient is necessary for MRI to record spatial map.

II. COMPONENTS OF MRS TECHNIQUE

Some of the integral components of MRS technology are radio-frequency source, gradients, slice selection, and phase encoding.

Radio Frequency Source

The RF coil is responsible for generating and broadcasting the RF energy. Specialized coils are used to provide improved resolution in the surface regions of the patient. It contains four main components: a frequency synthesizer, a digital envelope of RF frequencies, a high power amplifier, and a coil or antenna.

The final component of the RF system is the transmitter coil. Most MRS systems use a saddle coil to produce uniform RF fields over large volumes (e.g., body or head). This design is useful to produce uniform RF penetration and to generate an effective B_1 field perpendicular to B_0 even though the coil opening is parallel to B_0 . Two types of coil polarity are used, linearly polarized (LP) and circularly polarized (CP).

RF coils have two categories: volume and surface coil. Volume coils are typically cylindrical shaped, a popular example being a birdcage coil. Surface coils are subdivided into a single-loop coil or an array coil. Volume coils transmit and receive radio-frequency pulses and are called “trans-receivers.” Surface coils generally receive signals only and are traditionally used to improve signal-to-noise ratio. Unlike MRI studies, most spectroscopic measurements deposit little RF power to the patient, and specific absorption rate (SAR) limitations are infrequent in MRS due to long TR (repetition time) used in MR protocol. One

important exception is ^1H -decoupled MRS studies, which are particularly RF intensive and may be limited by RF heating concerns.

Gradient Coils

Gradient coils are used to apply gradients to the main B_0 field in X, Y, and Z directions. The gradient G_Z is applied along the long axis of the patient to select a slice (transverse section). This G_Z gradient is usually supplied by a pair of Helmholtz coils and has a typical value of $\approx 1 \text{ mT m}^{-1}$. The change in B_0 from one end of the patient to the other will be of the order 1:1000. The coils for G_Y and G_Z gradients are usually saddle shaped similar to the RF coils. These gradients allow the creation of a two-dimensional (2D) image of a particular slice. In practice, gradients can be applied in any desired direction by software control of the electronics. The gradients G_X , G_Y , and G_Z are generally switched on and off for a certain length of time in the complex pulse sequences of operations used for MRS studies. The mechanical stress produced on the various gradient coils by rapidly changing magnetic fields in MRS pulse sequences accounts for the strange noises often reported by patients undergoing MRS studies.

Gradient Methodology

The flow of electrical current through the gradient coils produces gradient fields. These gradient fields are applied in short bursts of pulses. The number, duration, and amplitude of the gradient pulse are determined by the particular pulse sequence and measurement parameters in the protocol. Continuous linear field homogeneity is made using gradient offset currents.

There are four characteristics to describe gradient system performance: maximum gradient strength; duty cycle; rise time and slew rate; and techniques for eddy current compensation. The major complication of gradient pulses for spectroscopic studies is eddy currents. Eddy currents are produced in response to a changing magnetic field (gradient pulse). Most eddy currents decay with shorter time constants compared with the time between the end of the gradient pulse and the beginning of data collection. Spectroscopic studies are particularly sensitive to eddy currents. In some instances, additional post-acquisition corrections are necessary to obtain well-resolved resonances.

Larger gradient strength allows for better spatial resolution. The duty cycle of the gradient amplifier is another important measure of gradient performance. The duty cycle determines how fast an amplifier can respond to the demands of a pulse sequence. Large

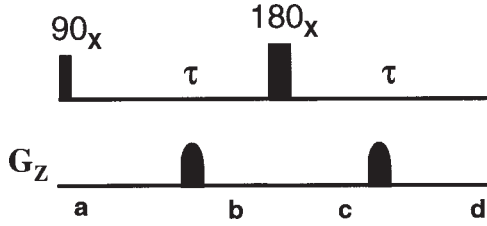


Figure 4 Application of pulsed field gradient to rephase transverse magnetization by 180° pulse and elimination of unwanted magnetization due to imperfect 180° . The gradients are placed symmetrically from the 180° pulse. Magnetization at various points (a–d) are explained in the text.

duty cycles allow high-amplitude gradient pulses between very short interpulse delays.

Selection of Magnetization by Gradients. Gradients are used extensively for two purposes, either rephasing (selection) (37) or dephasing (elimination) (38) of a particular magnetization transfer pathway (21). Whenever gradients are applied in a particular direction (for simplicity's sake, it is assumed here that gradients are applied along the Z direction), it generates a phase factor associated with the coherence level. It is convenient to re-express the Cartesian operators I_x and I_y in terms of raising and lowering operators I^+ and I^- , respectively, to describe the effects of field gradients to rephase transverse magnetization and removal of artifacts generated due to imperfect 180° pulse (38).

Rephasing of Transverse Magnetization. If two gradients with the same strength, shape, duration, and polarity are applied on either side of a 180° pulse, transverse magnetization is refocused (Fig. 4). Details of operator formalism are provided in the appendix (21). The rephasing of magnetization is an important application of gradients and it can be explained by analyzing the magnetization at different points in Fig. 4.

$$\begin{aligned}
 (a \rightarrow b) \quad I_z \xrightarrow{90^\circ} -I_y &= -\frac{1}{2i} [I^+ - I^-] \\
 &\xrightarrow{\gamma_1 \text{Gr}tL_z} -\frac{1}{2i} [I^+ e^{-i\gamma_1 \text{Gr}tL_z} - I^- e^{+i\gamma_1 \text{Gr}tL_z}] \\
 (b \rightarrow c) \quad \xrightarrow{180^\circ I_x} &-\frac{1}{2i} [I^- e^{-i\gamma_1 \text{Gr}tL_z} - I^+ e^{+i\gamma_1 \text{Gr}tL_z}] \\
 (c \rightarrow d) \quad \xrightarrow{\gamma_1 \text{Gr}tL_z} &-\frac{1}{2i} [I^- e^{-i\gamma_1 \text{Gr}tL_z} e^{+i\gamma_1 \text{Gr}tL_z} \\
 &- I^+ e^{-i\gamma_1 \text{Gr}tL_z} e^{+i\gamma_1 \text{Gr}tL_z}] = +\frac{1}{2i} [I^+ - I^-] \quad [1]
 \end{aligned}$$

The net phase acquired after 2τ is zero and we get back the same transverse magnetization ($I^+ - I^-$) that we started with, where G is the gradient strength, τ is the duration of gradient application, and r is the dis-

tance from the gradient isocenter. γ_H is the nuclear gyromagnetic ratio of proton.

Removal of Unwanted Magnetization Due to an Imperfect 180° Pulse. This application is critical to remove unwanted magnetization due to an imperfect 180° pulse and it can be explained by analyzing the magnetization at different points in Fig. 4.

$$\begin{aligned}
 (a \rightarrow b) \quad I_z \xrightarrow{90^\circ} -I_y &= -\frac{1}{2i} [I^+ - I^-] \\
 &\xrightarrow{\gamma_1 \text{Gr}tL_z} -\frac{1}{2i} [I^+ e^{-i\gamma_1 \text{Gr}tL_z} - I^- e^{+i\gamma_1 \text{Gr}tL_z}] \\
 (b \rightarrow c) \quad \frac{(180 + \theta) I_x}{\text{imperfect pulse}} &\rightarrow \\
 &-\frac{1}{2i} \text{Cos}\theta [I^+ e^{-i\gamma_1 \text{Gr}tL_z} - I^- e^{+i\gamma_1 \text{Gr}tL_z}] \\
 &\quad -\frac{1}{2} I_z [e^{-i\gamma_1 \text{Gr}tL_z} - e^{+i\gamma_1 \text{Gr}tL_z}] \\
 (c \rightarrow d) \quad \xrightarrow{-\gamma_1 \text{Gr}tL_z} &-\frac{1}{2i} \text{Cos}\theta [I^+ e^{-i\gamma_1 \text{Gr}tL_z} e^{+i\gamma_1 \text{Gr}tL_z} \\
 &- I^- e^{-i\gamma_1 \text{Gr}tL_z} e^{+i\gamma_1 \text{Gr}tL_z}] -\frac{1}{2i} \text{Cos}\theta \frac{1}{2i} [I^+ - I^-] \\
 &-\frac{1}{2} I_z [e^{-i\gamma_1 \text{Gr}tL_z} - e^{+i\gamma_1 \text{Gr}tL_z}] = -\frac{1}{2i} [I^+ - I^-] \\
 &\quad -\frac{1}{2} I_z [e^{-i\gamma_1 \text{Gr}tL_z} - e^{+i\gamma_1 \text{Gr}tL_z}] \quad [2]
 \end{aligned}$$

Any magnetization associated with a phase factor experiences different gradient strength, and the overall integrals become zero. Hence, at the end of 2τ , longitudinal magnetization (I_z) associated with the phase factor will be dephased.

Spatial Encoding and Slice Selection

In MRS, quantification of metabolites from a particular region of the body is the primary objective, and the selection of the specific region of the body is accomplished with the help of slice-selecting gradients, known as spatial encoding. Slice selection is achieved by applying a one-dimensional, constant magnetic field gradient. At the same time, a selective 90° pulse is applied. Application of this selective 90° pulse in conjunction with a magnetic field gradient will rotate spins that are located in a slice or a plane through the object.

Figure 5 illustrates the slice selection using application of a selective 90° pulse in the presence of field gradient G_z . The selective 90° pulse excites only a narrow frequency range ($\Delta\omega$), and this narrow tissue slice in the Z direction (ΔZ) is sampled for analysis as indicated by the shaded area in Fig. 5.

The magnitude of the slice select gradient determines the difference in precession frequency between the two points of the gradient. Steep gradient slopes

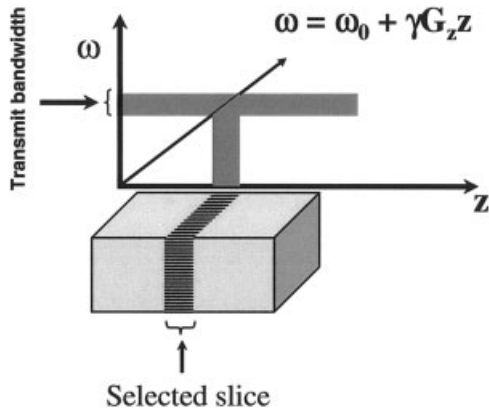


Figure 5 Selection of a slice using gradient.

generate a large difference in precession frequency between two points of the gradients, whereas shallow gradient slopes generate a small difference in precession frequency between the same two points (Fig. 6). Once a certain gradient slope is applied, then the RF pulse is transmitted to excite the slice that contains a range of frequencies between the two points. This frequency range is called bandwidth, and the RF being transmitted at this point is called the transmit bandwidth. Briefly, to achieve a thick slice, a shallow slice select gradient and/or a broad transmit bandwidth is applied (see Fig. 6A). To achieve a thin slice, a steep slice select gradient and/or narrow transmit bandwidth is applied (see Fig. 6B).

For example, in a 1.5 T magnet, water protons have a resonant frequency of approximately 64 MHz. For a 90° pulse with a frequency width of 1.0 kHz, the magnetic field gradient required to selectively excite a slice of tissue of 5 mm thick is calculated as follows:

$$\Delta\omega = \gamma\Delta B_z = \gamma G_z \Delta z, \quad \text{and} \quad \gamma = \frac{\omega}{B_z}, \quad [3]$$

Hence,

$$G_z = \frac{\Delta\omega}{\gamma\Delta z} = \frac{\Delta\omega B_z}{\omega \Delta z} = \frac{1.0}{64 \times 1000} \frac{1.5}{5 \times 10^{-3}} = \frac{1.5}{320} = 0.00468 \text{ Tm}^{-1}. \quad [4]$$

Figure 7A shows the orientation of different slices in a human brain. In general, we assume that the slice-selective gradient is applied along the Z direction and it generates an axial image (see Fig. 7B). However, for the sagittal and coronal images, G_x and G_y gradients are selected for slice selection gradients, respectively (see Fig. 7B).

Frequency Encoding. In a uniform B_0 field, after the application of a 90° pulse, the free induction

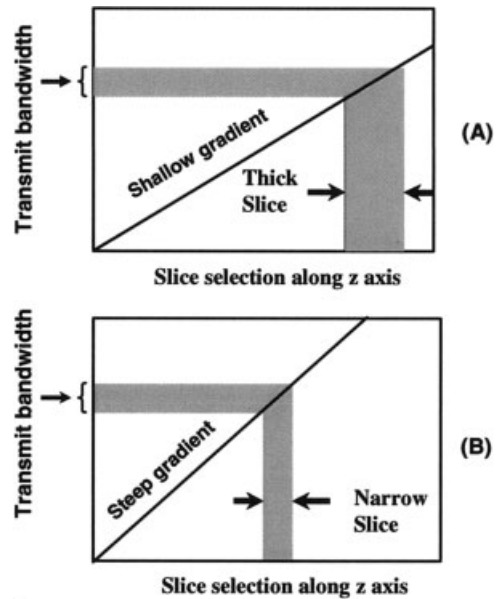


Figure 6 Selection of slice thickness with steepness of gradients. (A) Shallow gradient and (B) steep gradient.

decay (FID) with time contains all the necessary information for reconstructing the signal as a function of a frequency. This is accomplished with the help of Fourier transform (Fig. 8A).

Suppose we apply a 90° pulse after a field gradient along the X direction, G_x . This has the effect of “labeling” the spins and separates them according to distance along the X axis from the isocenter (see Fig. 8B). The resonant frequency at some point “X” along the linear field gradient relative to some reference point can be written as

$$\omega_x = \gamma X G_x. \quad [5]$$

The equation for the FID then becomes

$$f(t) = \int_x \rho(x) \exp(-i \gamma G_x x t) dx. \quad [6]$$

The Fourier transform of the FID converts from a frequency profile of signal intensity $F(\omega)$ to a spatial profile of signal intensity or spin density $\rho(x)$.

The frequency-encoding gradient is activated during signal acquisition and is often called the readout gradient. The echo is usually centered in the middle of the frequency-encoding gradient, so that the gradient is switched on during the rephasing and the dephasing part of the echo. The steepness of the slope of the frequency-encoding gradient determines the size of the anatomy covered along the frequency-encoding axis during a scan.

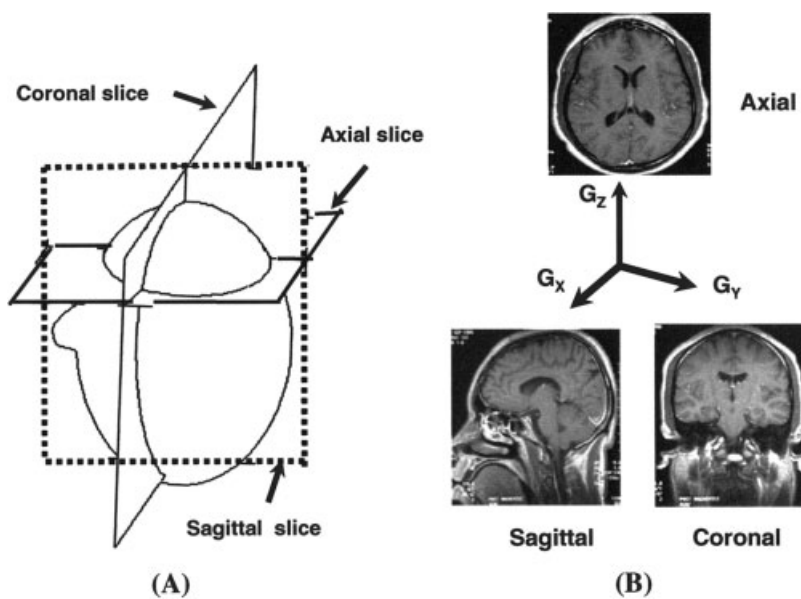


Figure 7 (A) The use of different physical gradients for selecting slice in the brain. (B) Three images (axial, sagittal, and coronal) are generated due to different slice selection (G_z , G_x , and G_y) gradients.

The resolution of the image along the X axis depends on a number of points used for sampling (typically 256 points in a field of view of 20–40 cm). In MRS, nuclei (^1H , ^{31}P , etc.) precess in different frequencies depending on chemical environments and this is why the application of frequency encoding gradients is not necessary in MRS. This is a major difference between MRI and MRS experiments.

Phase Encoding. The process of locating an MR signal by altering the phase of spins using a magnetic

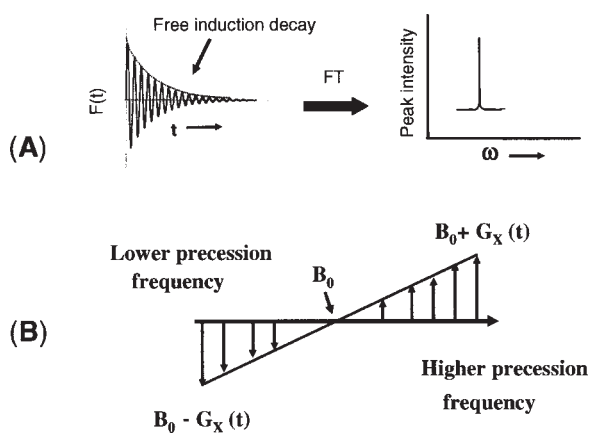


Figure 8 (A) Conversion of free induction decay to spectra using Fourier transformation. (B) Pictorial representation of the effective magnetic field experiencing different spins depending on the location.

field gradient along a particular dimension prior to the acquisition of the signal is called phase encoding. If a gradient field is briefly switched on and then switched off with predefined altered amplitude before acquisition of data, the magnetization of the external voxels will either precess faster or slower relative to the amplitude of the phase encoding gradient (Fig. 9). The steepness of the slope of the phase-encoding gradient determines the degree of phase shift between two points along the gradient axis. A steep phase-encoding gradient causes a large phase shift between two points along the gradient, whereas a shallow phase-encoding gradient causes a smaller phase shift between the same two points along the gradient. Some essential concepts of spatial encoding are

- The phase-encoding gradient alters the phase along the remaining axis of the image, which is usually the short axis of the anatomy.
- In coronal images, the short axis of the anatomy usually lies along the horizontal axis of the magnet, and therefore the X gradient performs the phase encoding.
- In sagittal images, the short axis of the anatomy usually lies along the vertical axis of the magnet, and therefore the Y gradient performs the phase encoding.
- In axial images, the short axis of the anatomy usually lies along the vertical axis of the magnet, and therefore the Y gradient performs the

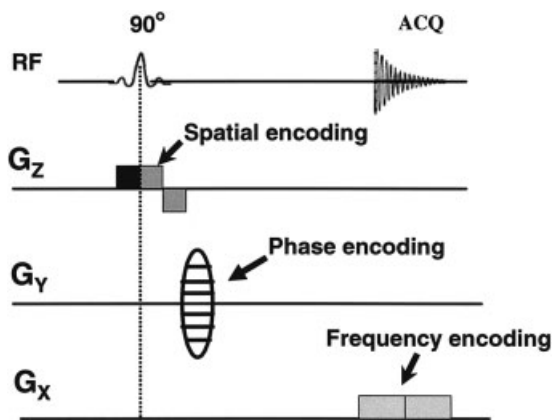


Figure 9 Representation of spatial, phase, and frequency encoding in a typical MRI sequence. The frequency-encoding gradients are not applied in MRS pulse sequences.

phase encoding. However, when imaging the head, the short axis of the anatomy lies along the horizontal axis of the magnet, and therefore the X gradient performs the phase encoding.

A field gradient is applied along the Y direction, G_y as a short pulse, after the RF pulse, but before the main acquisition time of the FID. This has the effect of progressively phase shifting the precessing spins along the Y direction, but without changing the frequency. This labels the spins in a different way, but to disentangle all the information, the computing procedure used to reconstruct the second dimension in the 2D slice requires that the operation be performed in many steps (typically 256) where the phase encoding amplitude is varied incrementally. This particular process determines the resolution in the Y direction, and largely accounts for the long time needed for the whole imaging experiment.

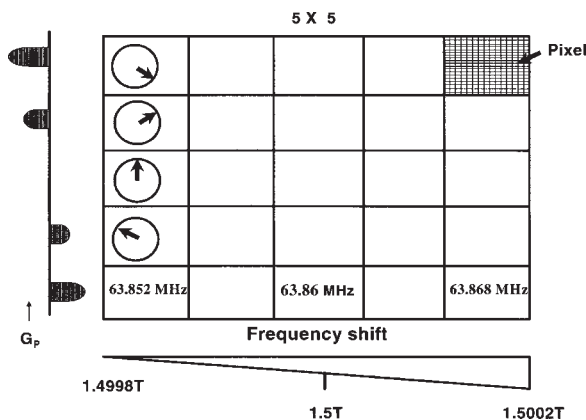


Figure 10 A graphical representation of the frequency (X axis) and phase encoding (Y axis). The amplitude of the phase-encoding gradient changes sequentially.

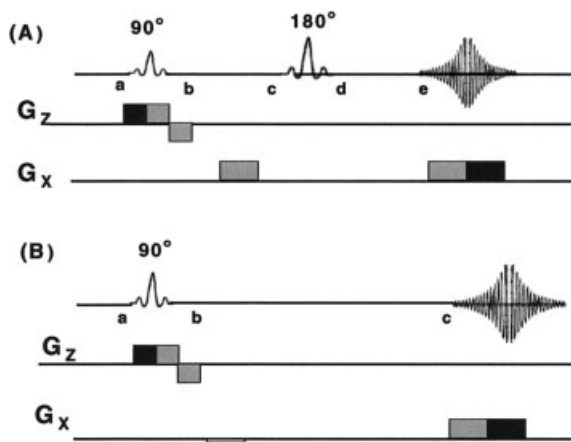


Figure 11 Pulse sequences for (A) spin echo and (B) gradient echo. Magnetization at different points is described in the text.

In the frequency domain (X axis) (Fig. 10), there is a change in frequency depending on the location of the voxel. In Figure 10, we have assumed that our area of interest is subdivided into 5×5 matrices. The amplitude of the phase gradient varies systematically; as the amplitude varies, the phase of the spin varies differently as depicted along the phase shift axis. Frequency encoding is applied in MRS, and it is provided by the inherent chemical shift differences of different spins.

Formation of an Image

After getting an image of the brain, a voxel is chosen in the region of interest for MRS analysis. Generally, two MRI sequences (e.g., a spin echo or a gradient echo) are applied for generating an MRI image. A detailed discussion about these two sequences is given below.

Spin Echo (SE). A spin echo uses a 90° RF pulse along with a slice-selective gradient (Fig. 11A). This selective 90° excitation pulse flips the magnetization within the slice to the transverse plane and magnetization is dephased by the first gradient. A 180° pulse is applied at the middle of the sequence and the magnetization is rephased by the second gradient. The amplitude of the spin echo is affected by T_2 relaxation; the resulting images are T_2 weighted. The degree of T_2 weighting is determined by the value of TE, which may vary from few milliseconds to hundreds of milliseconds.

SE sequence employs large flip angles, so it requires long recovery time (TR) to allow adequate recovery of longitudinal magnetization. Typically, TR values range from hundreds of milliseconds to

seconds. As total scan time is dependent on TR; a SE sequence can be lengthy. Spin echo is the least artifact-prone sequence and generates a high signal-to-noise ratio. However, SAR is higher in SE due to both 90° and 180° RF pulses. Long TR in SE sequence times is incompatible with 3D acquisitions.

In SE (see Fig. 11A), magnetization at different points are explained as follows:

$$\begin{aligned}
 (a \rightarrow b) \quad I_z &\xrightarrow{90^\circ} I_x = \frac{1}{2}[I^+ + I^-] \\
 &\xrightarrow{G_x\tau} \frac{1}{2}[I^+e^{-iG_x\tau} - I^-e^{+iG_x\tau}] \\
 &\xrightarrow{-G_x\tau} \frac{1}{2}[I^+e^{-iG_x\tau}e^{+iG_x\tau} - I^-e^{+iG_x\tau}e^{-iG_x\tau}] \\
 &= \frac{1}{2}[I^+ - I^-] \\
 (b \rightarrow c) \quad &\xrightarrow{+G_x\tau} \frac{1}{2}[I^+e^{-iG_x\tau} - I^-e^{+iG_x\tau}] \\
 (c \rightarrow d) \quad &\xrightarrow{180^\circ} \frac{1}{2}[I^-e^{-iG_x\tau} - I^+e^{+iG_x\tau}] \\
 &\xrightarrow{G_x\tau} \frac{1}{2}[I^-e^{+iG_x\tau}e^{-iG_x\tau} + I^+e^{+iG_x\tau}e^{-iG_x\tau}] \\
 &= \frac{1}{2}[I^+ + I^-] = \text{Echo} \quad [7]
 \end{aligned}$$

Gradient Echo (GE). A GE pulse sequence (see Fig. 11B) uses a variable RF excitation pulse (generally less than 90°). Hence, the magnitude of transverse magnetization is less than spin echo, where all the longitudinal magnetizations are converted to a transverse plane. After the RF pulse is applied, the magnetization in the transverse plane is dephased by the gradient and then rephased by the second gradient. The term TE is the interval between RF excitation and the center of the gradient echo. The value of TE is important in determining the signal contrast of the image. As the transverse magnetization is subject to T₂ dephasing, regions of tissue whose T₂ value is short compared with TE will exhibit greatly attenuated signals. By contrast, regions with longer T₂ will have somewhat higher signals.

GE sequence often employs very short TR values, and images exhibit T₁ weighting. Tissue with short T₁ appears brighter because their longitudinal magnetization is less easily saturated. The degree of T₁ weighting also increases with flip angle, because higher flip angles cause greater saturation. The flip angle typically used in GE is within the range of 20°–45°. GE can provide faster imaging using shorter TR and shorter TEs than spin echo. In GE, less energy deposit occurs in the body due to use of low flip angle (>90°). In GE, more slices per TR are generated than SE. GE is more compatible with 3D acquisitions. Chemical shifts are

not refocused in GE, and this is the most important difference with a SE sequence.

In GE (see Fig. 11B), magnetization at different points are explained as follows:

$$\begin{aligned}
 (a \rightarrow b) \quad I_z &\xrightarrow{90^\circ} -I_y = -\frac{1}{2i}[I^+ - I^-] \\
 &\xrightarrow{G_x\tau} -\frac{1}{2i}[I^+e^{-iG_x\tau} - I^-e^{+iG_x\tau}] \\
 &\xrightarrow{-G_x\tau} -\frac{1}{2i}[I^+e^{-iG_x\tau}e^{+iG_x\tau} \\
 &\quad - I^-e^{+iG_x\tau}e^{-iG_x\tau}] = -\frac{1}{2i}[I^+ - I^-] \\
 (b \rightarrow c) \quad &\xrightarrow{G_x\tau} -\frac{1}{2i}[I^+e^{-iG_x\tau} - I^-e^{+iG_x\tau}] \\
 &\xrightarrow{-G_x\tau} -\frac{1}{2i}[I^+e^{-iG_x\tau}e^{+iG_x\tau} - I^-e^{+iG_x\tau}e^{-iG_x\tau}] \\
 &= -\frac{1}{2i}[I^+ - I^-] = \text{Gradient echo.} \quad [8]
 \end{aligned}$$

Gradient and spin-echo-generated images are usually modulated by relaxation properties (T₁ and T₂) of ¹H nuclei in the region of interest. Images are categorized into two types (e.g., T₁ weighted or T₂ weighted).

T₁-Weighted Images. T₁-weighted images are produced using either the spin SE or the GE sequences. For T₁-weighted images, short TR and short TE are used to enhance the T₁ differences between tissues. T₁-weighted images have excellent contrasts (e.g., fluids are very dark, unless they are fast moving, water-based tissues are midgrey, and fat-based tissues are usually very bright). T₁-weighted images are often known as anatomy scans (Fig. 12A).

T₂-Weighted Images. T₂-weighted images are produced by SE or GE sequences, but GE images are affected by the magnetic field inhomogeneity. SE T₂ images require a long TR, a long TE, and take longer to acquire than T₁-weighted images (scan time depends directly on the TR). In these scans, fluids have the highest intensity, whereas water- and fat-based tissues are mid-gray. T₂ images are often thought of as pathology scans because collections of abnormal fluid are bright against the darker normal tissues (see Fig. 12B).

III. TECHNICAL ISSUES

MRS is performed as an adjunct to MRI. An MRI image is first generated, the voxel is selected at the site of interest, and then MRS spectra recorded from that voxel. The use of spatial localization is essential for in vivo MRS for selection of single voxel from a particular region of interest. Multiple-voxel techniques, popularly known as chemical shift imaging,

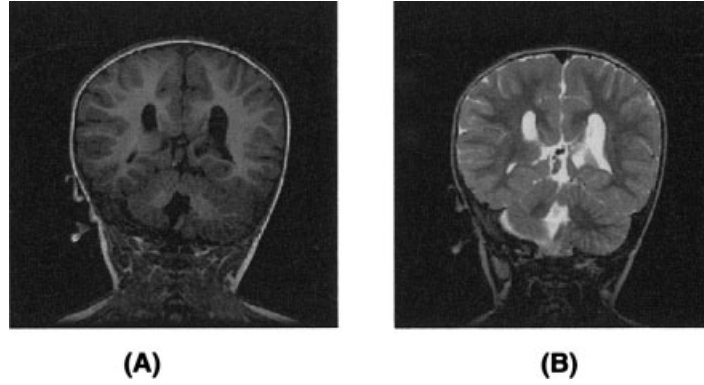


Figure 12 Conventional spin echo (A) T_1 and (B) T_2 -weighted images of brain.

allow simultaneous acquisition of in vivo MR spectra from several voxels in one experiment.

Spatial Localization Based on Single-Voxel Technique

The most frequently used localization methods for ^1H MRS of the brain are PRESS (point-resolved spectroscopy) (2) and STEAM (stimulated echo acquisition mode) (39). The basic principle underlying single-voxel technique is to use three mutually orthogonal slice selective pulses and design the pulse sequence to collect only the echo signal from the point (voxel) in space where all three slices intersect (Fig. 13). PRESS pulse sequence (Fig. 14) creates a double spin echo from the pulse sequence.

$$90^\circ \rightarrow \text{TE}/2 \rightarrow 180^\circ \rightarrow \text{TE}/2 \rightarrow [\text{Echo 1}] \rightarrow \text{TE}/2 \rightarrow 180^\circ \rightarrow \text{TE}/2 \rightarrow [\text{Echo 2}] \quad [9]$$

where TE is the echo time. The magnetization at different points for the PRESS sequence (see Fig. 14) is shown in Eq. [10] as follows:

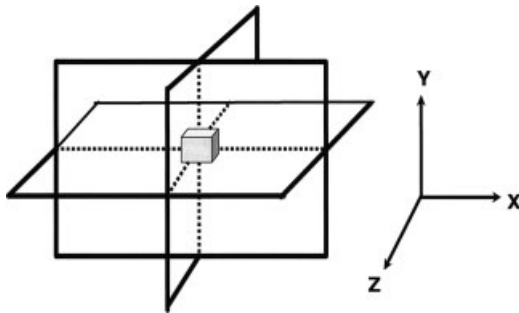


Figure 13 A schematic illustration of selecting a voxel by three orthogonal slice-selecting pulse used in STEAM or PRESS pulse sequences. The size and position of the voxel is controlled by the frequency and bandwidth of the slice-selecting pulses, as well as the amplitude of the associated slice-selecting gradients.

$$\begin{aligned}
 (a \rightarrow b) \quad I_z &\xrightarrow{90^\circ} I_x = \frac{1}{2} [I^+ + I^-] \\
 &\xrightarrow{G_x \tau} \frac{1}{2} [I^+ e^{-iG_x \tau} + I^- e^{+iG_x \tau}] \\
 &\xrightarrow{-G_x \tau} \frac{1}{2} [I^+ e^{-iG_x \tau} e^{+iG_x \tau} \\
 &\quad + I^- e^{+iG_x \tau} e^{-iG_x \tau}] = \frac{1}{2} [I^+ + I^-] \\
 (b \rightarrow c) \quad \frac{1}{2} [I^+ + I^-] &\xrightarrow{\text{Chem. shift}} \frac{1}{2} [I^+ e^{i\Omega_H \text{TE}/2} + I^- e^{-i\Omega_H \text{TE}/2}] \\
 (c \rightarrow d) \quad \frac{G_x \tau}{2} &\left[I^+ e^{-iG_x \tau} e^{i\Omega_H \text{TE}/2} + I^- e^{+iG_x \tau} e^{-i\Omega_H \text{TE}/2} \right] \\
 &\frac{1}{2} \left[I^- e^{-iG_x \tau} e^{i\Omega_H \text{TE}/2} + I^+ e^{+iG_x \tau} e^{-i\Omega_H \text{TE}/2} \right] \\
 &\xrightarrow{G_x \tau} \frac{1}{2} \left[I^- e^{-iG_x \tau} e^{+iG_x \tau} e^{i\Omega_H \text{TE}/2} \right. \\
 &\quad \left. + I^+ e^{+iG_x \tau} e^{-iG_x \tau} e^{-i\Omega_H \text{TE}/2} \right] \\
 &= \frac{1}{2} [I^- e^{i\Omega_H \text{TE}/2} + I^+ e^{-i\Omega_H \text{TE}/2}] \\
 (d \rightarrow e) \quad \frac{\text{Chem. shift}}{\text{TE}/2} &\rightarrow \frac{1}{2} [I^- e^{i\Omega_H \text{TE}/2} e^{-i\Omega_H \text{TE}/2} \\
 &\quad + I^+ e^{-i\Omega_H \text{TE}/2} e^{+i\Omega_H \text{TE}/2}] \\
 &= \frac{1}{2} [I^- + I^+] \rightarrow \text{Echo 1} \\
 (e \rightarrow f) \quad \frac{\text{Chem. shift}}{\text{TE}/2} &\frac{1}{2} [I^+ e^{i\Omega_H \text{TE}/2} + I^- e^{-i\Omega_H \text{TE}/2}] \\
 (f \rightarrow g) \quad \frac{1}{2} &\left[I^- e^{i\Omega_H \text{TE}/2} + I^+ e^{-i\Omega_H \text{TE}/2} \right] \\
 (g \rightarrow h) \quad \frac{1}{2} &[I^- + I^+] \rightarrow \text{Echo 2.} \quad [10]
 \end{aligned}$$

Hence, at the time of data acquisition, we get back the same magnetization as we started with at point b.

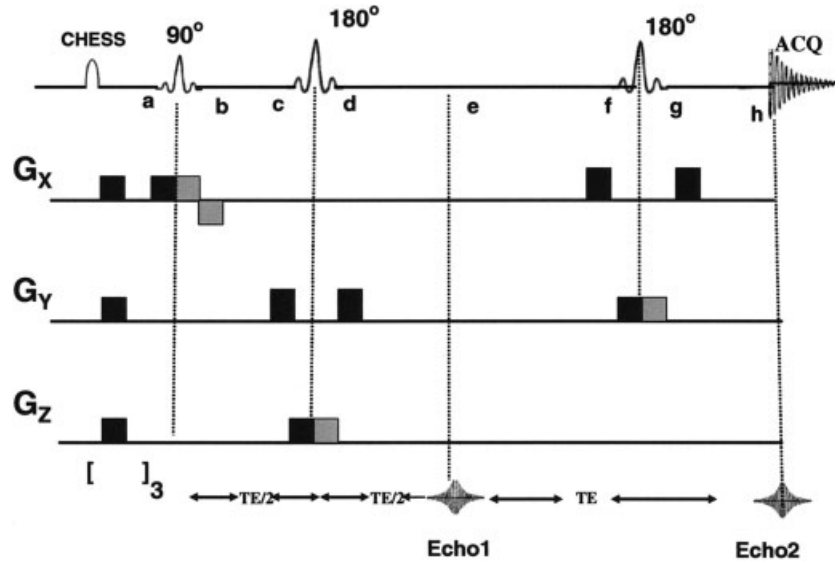


Figure 14 A schematic diagram of PRESS pulse sequence. Magnetization at different points is described in the text. Chemical shift selective imaging (CHESS) pulses at the beginning of the pulse sequence are used to suppress water peak (98). []₃ symbol at the bottom indicates frequency-selective 90° pulse to selectively excite the water, followed by application of spoiler gradient (repeated thrice) to dephase the resulting magnetization.

Thus, sensitivity is not lost in a PRESS sequence. However, PRESS is a longer pulse sequence.

STEAM pulse sequence selects a stimulated echo from the pulse sequence (Fig. 15). The general pulse sequence scheme for STEAM is given below.

$$90^\circ \rightarrow TE/2 \rightarrow 90^\circ \rightarrow TM \rightarrow 90^\circ \rightarrow TE/2 \rightarrow \text{“[Echo]”} \quad [11]$$

where TM is the mixing time. The magnetization at different points originated from STEAM sequence (see Fig. 15) are given in Eq. [12] as follows:

$$\begin{aligned} (a \rightarrow b) \quad I_z &\xrightarrow{90^\circ_x} = I_y. -\frac{1}{2i} [I^+ - I^-] \xrightarrow{G_x \tau} \\ &-\frac{1}{2i} [I^+ e^{-iG_x \tau} - I^- e^{+iG_x \tau}] \\ &\xrightarrow{-G_x \tau} -\frac{1}{2i} [I^+ e^{-iG_x \tau} e^{+iG_x \tau} - I^- e^{+iG_x \tau} e^{-iG_x \tau}] \\ &= -\frac{1}{2i} [I^+ - I^-] \\ (b \rightarrow c) \quad \frac{\text{Chem. shift}}{TE/2} &\rightarrow -\frac{1}{2i} [I^+ e^{i\Omega_H TE/2} \\ &- I^- e^{-i\Omega_H TE/2}] \\ (c \rightarrow d) \quad \xrightarrow{-G_x \tau} &-\frac{1}{2i} [I^+ e^{+iG_x \tau} e^{i\Omega_H TE/2} \\ &- I^- e^{-iG_x \tau} e^{-i\Omega_H TE/2}] \end{aligned}$$

$$\begin{aligned} &\xrightarrow{G_x \tau} -\frac{1}{2i} [I^+ e^{i\Omega_H TE/2} - I^- e^{-i\Omega_H TE/2}] \\ &= \xrightarrow{90^\circ_x} -\frac{1}{2i} [e^{i\Omega_H TE/2} \left\{ \frac{1}{2} (I^+ + I^-) + iI_z \right\} \\ &\quad - e^{-i\Omega_H TE/2} \left\{ \frac{1}{2} (I^+ + I^-) + iI_z \right\}] \\ (d \rightarrow e) \quad \frac{G_x^1 \tau_1}{\text{Spoiler}} &-\frac{1}{2i} [e^{i\Omega_H TE/2} \{ +iI_z \} \\ &\quad - e^{-i\Omega_H TE/2} \{ -iI_z \}] \\ (e \rightarrow f) \quad \xrightarrow{90^\circ_x} &-\frac{1}{2i} [e^{i\Omega_H TE/2} \{ (I^- - I^+) \} \\ &+ e^{-i\Omega_H TE/2} \{ (I^- - I^+) \}] \\ \frac{G_x \tau}{-G_x \tau} &= -\frac{1}{2i} [e^{i\Omega_H TE/2} \{ (I^- - I^+) \} \\ &+ e^{-i\Omega_H TE/2} \{ (I^- - I^+) \}] \\ (f \rightarrow g) \quad \frac{\text{Chem. shift}}{TE/2} &\rightarrow +\frac{1}{2i} [I^+ - I^-] \\ &-\frac{1}{2i} [I^- e^{-i\Omega_H TE} - I^+ e^{-i\Omega_H TE}] = \frac{1}{2i} [I^+ - I^-] \\ &= \text{Reduced signal intensity.} \quad [12] \end{aligned}$$

Hence, at the time of data acquisition, we get half the magnetization that we started with at point b. Thus, in a STEAM sequence, sensitivity is reduced by half. Figure 16 shows the ¹H MRS data acquired

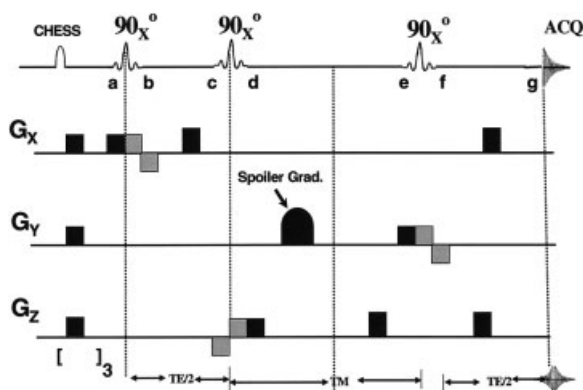


Figure 15 A schematic diagram of STEAM pulse sequence. Magnetization at different points is described in the text. Chemical shift selective imaging (CHES) pulses at the beginning of the pulse sequence are used to suppress water peak (98). $[]_3$ symbol at the bottom indicates frequency-selective 90° pulse to selectively excite the water, followed by application of spoiler gradient (repeated thrice) to dephase the resulting magnetization.

in the same region by PRESS and STEAM sequences at 3T magnetic field (40).

Similarities between PRESS and STEAM

- Both of these pulse sequences involve sequential application of three orthogonal gradients to select slices, during which selective RF pulses are used to excite the spins in each slice. Hence, at the end of the three-slice series, the only spins excited are within the chosen volumes.
- Both PRESS and STEAM can be applied along with the phase-encoding gradients, which allow the defined volumes to be subdivided. This yields a signal acquisition from multiple volumes simultaneously. Because the metabolite distribution can be represented as maps, this approach is known as magnetic resonance spectroscopic imaging (MRSI) or chemical shift imaging (CSI) (24, 41–43).

Differences between PRESS and STEAM

- In a PRESS sequence, sensitivity is higher by a factor of two than a STEAM sequence, given the same echo time. This is because the stimulated echo is formed from only half the available equilibrium magnetization.
- The STEAM sequence is less sensitive to T_2 -relaxation effects as no T_2 relaxation occurs during the mixing time, whereas PRESS is

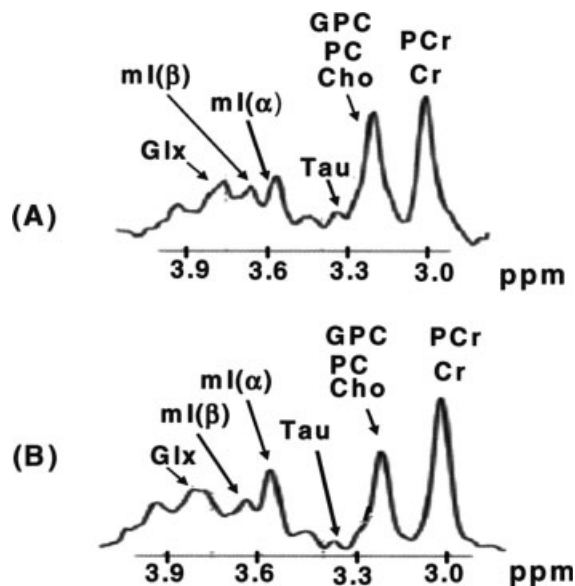


Figure 16 A comparison of the brain spectra at 3T using (A) PRESS and (B) STEAM pulse sequences. The in vivo acquisition spectra shown are from the occipital region of a 22-year-old healthy male. For all acquisitions, the bandwidth was 2.5 kHz with the collection of 2,048 data points. A line width broadening function of ~ 6 Hz was applied to simulate the in vivo line width (99).

sensitive to T_2 -relaxation throughout the localization sequence. STEAM has two echo intervals; PRESS has four echo intervals.

- With the same hardware, shorter TEs can be achieved with STEAM than with PRESS.
- STEAM may have slightly better water suppression factor, because water suppression pulses can be added during the TM period (which does not occur in PRESS). In addition, STEAM may have less spurious water signals from the 90° slice selective pulses than the 180° pulses in PRESS.
- Another factor to consider, especially at higher field strengths, is that the amount of power deposited (i.e., SAR) is approximately twice as high for PRESS compared with STEAM. SAR is not a significant factor at low fields (e.g., 1.5 T). The Federal Drug Administration has approved higher fields (up to 3.0 T) for clinical use. At present, 7.0 T scanners are being used exclusively for research purposes.

Chemical Shift Imaging (CSI)

Chemical shift imaging (CSI) or magnetic resonance spectroscopic imaging (MRSI) is an efficient technique for noninvasive characterization and quantification of metabolites from simultaneous acquisition

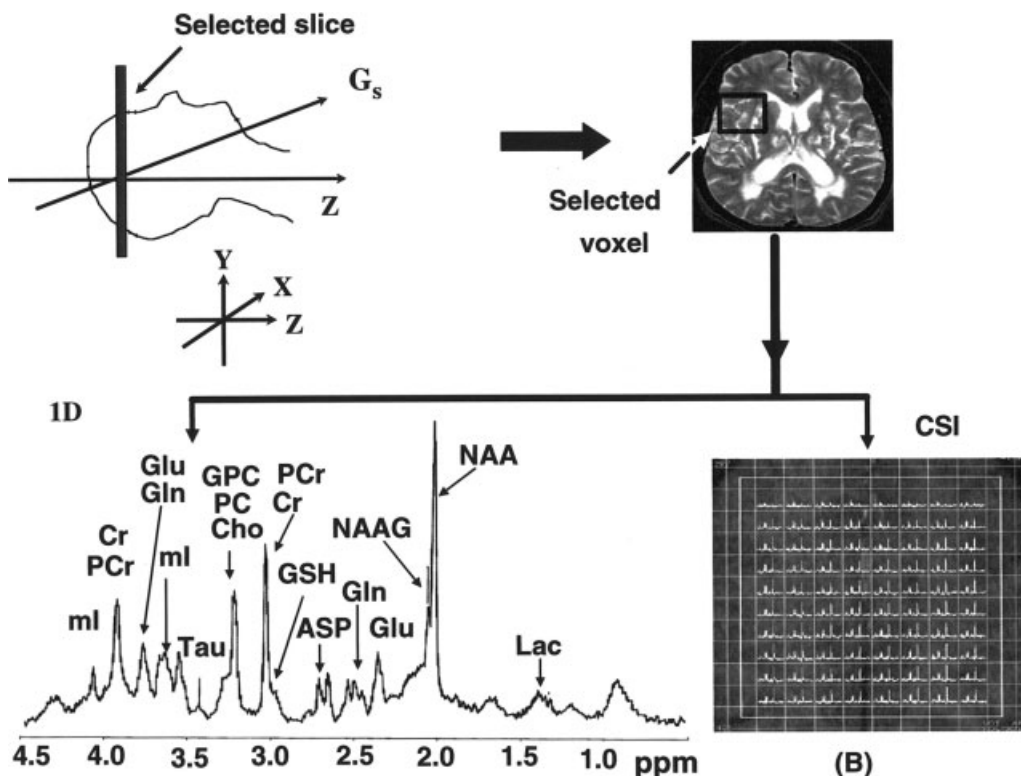


Figure 17 A pictorial representation of the scheme involving one-dimensional (1D) and chemical shift imaging (CSI) MRS study. Initial steps are to place the subject into the scanner, adjusting the power level and shimming and recording MRI images. Voxel is then selected in the desired location of the brain. Depending on the nature of the study, desired MRS pulse sequences are used for one-dimensional (1D) single-voxel MRS (A) or multivoxel CSI (B) spectra of the brain.

of spectra from multiple voxels. Phase encoding can be used either with a simple FID acquisition or in combination with volume selective methods, such as PRESS or STEAM. Because frequency encoding is not possible in spectroscopy, phase encoding must be applied in each of the directions in which spatial information is required—namely, two directions for 2D chemical shift imaging or three directions for 3D CSI. Scan time is dependent on the number of voxels (N) in a particular direction. Given that, each phase-encoding step requires a separate TR period, and the scan time increases as N^2 for 2D or N^3 for 3D CSI. Because the scan time increases so rapidly with N , this imposes a further constraint on spatial resolution. In multivoxel ^1H MRS, typical in-plane resolutions are in the order of 1 to 2 cm. In ^{31}P MRS, even lower resolutions are used because of the lower sensitivity of the ^{31}P nucleus.

The information collected in a multivoxel acquisition can be presented as an array of spectra (Fig. 17B). The metabolite maps can be displayed in color and overlaid on an MR image of the same slice.

One advantage to this technique is that there is no chemical shift artifact problem as seen in single- or multiple-voxel localization techniques. Therefore, it is useful for high-field in vivo MRS applications in which the chemical shift dispersion is linearly increased as a function of B_0 .

A major technical problem is the difficulty of shimming an entire slice to the level necessary for good spectra from every voxel in the matrix. When setting up a CSI scan, the edges of the region of interest should lie within the skull to avoid the susceptibility changes associated with the bone.

Comparison of Single-Voxel versus Multiple-Voxel Techniques. Usually, but not exclusively, in a single-voxel spectroscopy (SVS) technique, scans are recorded at short TEs (35 ms), whereas multiple voxel techniques, such as MRSI studies, are performed at long TEs (e.g., TE > 135 ms). In SVS, spectra contain signals from more compounds and have better SNRs, but also have worse water and lipid contamination. In MRSI, spectra have lower SNR,

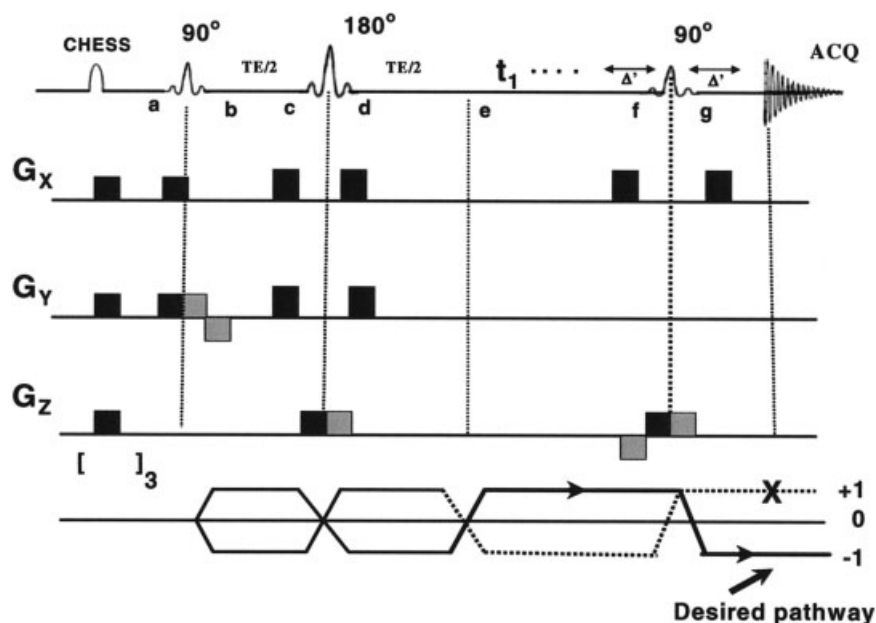


Figure 18 A schematic diagram of a two-dimensional L-COSY pulse sequence. The RF pulse scheme consisted of three RF pulses (90° , 180° , 90°) that were slice-selective along three orthogonal axes. A pair of B_0 gradient crusher pulses were symmetric with respect to the slice-refocusing 180° RF pulse. The last slice-selective 90° RF pulse with a pair of symmetric B_0 gradient crushers also served as a coherence transfer pulse for the L-COSY spectrum. The coherence transfer pathway diagram depicts the different stages of conversion of magnetization/coherences. Chemical shift-selective imaging (CHES) pulses at the beginning of the pulse sequence are used to suppress water peak (98). $[]_3$ symbol at the bottom indicates frequency-selective 90° pulse to selectively excite the water, followed by application of spoiler gradient (repeated thrice) to dephase the resulting magnetization.

fewer detectable compounds, and variable amounts of T_2 weighting but are usually better-resolved spectra with flatter baselines. SVS takes less time than MRSI studies. Resolution in SVS is higher than MRSI techniques. Quantification of metabolites is more robust in SVS compared with MRSI techniques.

Two-Dimensional Technique

A major concern with one-dimensional MRS is that many peaks overlap, and precise quantification is not possible. In particular, the dominant peaks of glutathione (GSH) overlap with other metabolites. Spectral editing and multiple-quantum (MQ) techniques can be used to differentiate glutathione and Glx metabolites from overlapping lipids signals (44–47). A drawback of the spectral editing technique is that only one metabolite can be selectively detected (44, 45). Reduced signal strength of metabolites is a major concern with MQ techniques (46, 47). Several versions of localized 2D MRS sequences (Fig. 18) have been successfully implemented on whole-body

1.5 T and 3 T MR imaging scanners (48, 49). Due to an added dimension, a localized 2D MR spectrum has better resolution (Fig. 19) than a conventional 1D MR spectrum (48, 49).

A 2D L-COSY sequence is operated on a single voxel. Two major problems (49) yet to be resolved in the localized 2D MR spectroscopy are (1) minimizing the RF pulses used for localization and coherence transfer, taking into consideration that some of the brain metabolites have short T_2 ; and (2) recording the localized 2D spectra of human organs in a reasonable time duration.

Prior to localization by the 2D L-COSY sequence, a CHES sequence consisting of three frequency-selective water-suppression pulses with a bandwidth of approximately 75 Hz was used, each followed by the dephasing B_0 gradient pulses.

The 2D L-COSY pulse sequence had a combination of three slice-selective RF pulses (90° – 180° – 90°) to localize a desired voxel. The desired coherence transfer pathways selected by a pair of gradient pulses are also shown along with the pulse sequence (see Fig. 18).

The magnetization at different points of a 2D-L-COSY sequence is given in Eq. 13 as follows:

$$\begin{aligned}
(a \rightarrow b) \quad I_Z &\xrightarrow{90_x} -I_Y = -\frac{i}{2}[I^- - I^+] \xrightarrow{G_y \tau} \\
&-\frac{i}{2}[I^- e^{+iG_y \tau} - I^+ e^{-iG_y \tau}] \\
&\xrightarrow{-G_y \tau} -\frac{i}{2}[I^+ e^{+iG_y \tau} e^{-iG_x \tau} - I^+ e^{-iG_y \tau} e^{+iG_y \tau}] \\
&= -\frac{i}{2}[I^- - I^+] \\
(b \rightarrow e) \quad \frac{\text{Chem. shift}}{TE/2} &\rightarrow -\frac{i}{2}[I^- e^{-i\Omega_H TE/2} - I^+ e^{+i\Omega_H TE/2}] \\
(c \rightarrow d) \quad \xrightarrow{G_z \tau} &-\frac{i}{2}[I^- e^{+iG_z \tau} e^{-i\Omega_H TE/2} - I^+ e^{-iG_z \tau} e^{+i\Omega_H TE/2}] \\
&\xrightarrow{180_x} -\frac{i}{2}[I^+ e^{+iG_z \tau} e^{-i\Omega_H TE/2} - I^- e^{-iG_z \tau} e^{+i\Omega_H TE/2}] \\
&\xrightarrow{G_z \tau} -\frac{i}{2}[I^+ e^{+iG_z \tau} e^{-iG_z \tau} e^{-i\Omega_H TE/2} \\
&- I^- e^{-iG_z \tau} e^{+iG_z \tau} e^{+i\Omega_H TE/2}] \\
&= -\frac{i}{2}[I^- e^{-i\Omega_H TE/2} - I^+ e^{+i\Omega_H TE/2}] \\
(d \rightarrow e) \quad \frac{\text{Chem. shift}}{TE/2} &\rightarrow -\frac{i}{2}[I^- e^{-i\Omega_H TE/2} e^{+i\Omega_H TE/2} \\
&- I^+ e^{+i\Omega_H TE/2} e^{-i\Omega_H TE/2}] = -\frac{i}{2}[I^- - I^+] \\
(e \rightarrow f) \quad \frac{\text{Chem. shift}}{t_1} &= -\frac{i}{2}[I^- e^{+i\Omega_H t_1} - I^+ e^{-i\Omega_H t_1}] \\
&\quad \text{Spin - Spincoupling} \\
&\quad t_1 \\
&-\frac{i}{2}[I^- e^{i\Omega_H t_1} \{\cos(\pi J_{IS} t_1) + 2iS_Z \sin(\pi J_{IS} t_1)\}] \\
&+\frac{i}{2}[I^+ e^{-i\Omega_H t_1} \{\cos(\pi J_{IS} t_1) - 2iS_Z \sin(\pi J_{IS} t_1)\}] \\
(f \rightarrow g) \quad \xrightarrow{-G_z \tau} &-\frac{i}{2}[I^- e^{i\Omega_H t_1} e^{-iG_z \tau} \{\cos(\pi J_{IS} t_1) \\
&+ 2iS_Z \sin(\pi J_{IS} t_1)\}] \\
&+\frac{i}{2}[I^+ e^{-i\Omega_H t_1} e^{+iG_z \tau} \{\cos(\pi J_{IS} t_1) - 2iS_Z \sin(\pi J_{IS} t_1)\}] \\
&\xrightarrow{+G_z \tau} -\frac{i}{2}[I^- e^{i\Omega_H t_1} e^{-iG_z \tau} e^{+iG_z \tau} \{\cos(\pi J_{IS} t_1) \\
&+ 2iS_Z \sin(\pi J_{IS} t_1)\}] \\
&+\frac{i}{2}[I^+ e^{-i\Omega_H t_1} e^{+iG_z \tau} e^{-iG_z \tau} \{\cos(\pi J_{IS} t_1) \\
&+ 2iS_Z \sin(\pi J_{IS} t_1)\}] \\
&= -\frac{i}{2}[I^- e^{i\Omega_H t_1} \{\cos(\pi J_{IS} t_1) + 2iS_Z \sin(\pi J_{IS} t_1)\}] \\
&+\frac{i}{2}[I^+ e^{-i\Omega_H t_1} \{\cos(\pi J_{IS} t_1) - 2iS_Z \sin(\pi J_{IS} t_1)\}] \\
&= \text{Data acquisition (during } t_2). \quad [13]
\end{aligned}$$

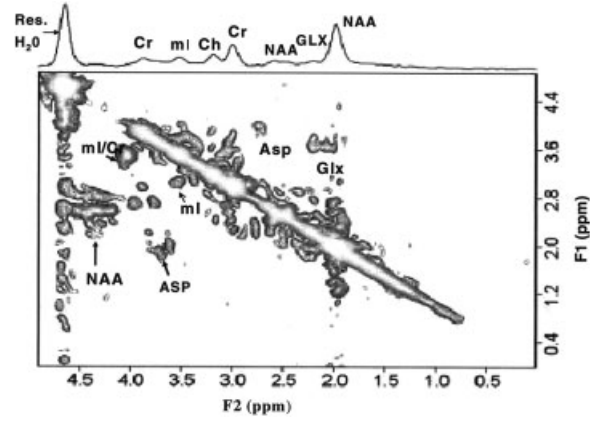


Figure 19 2D L-COSY MR spectrum of a 27-year-old healthy control in the occipito-parietal gray matter region at 1.5 T scanner. The 2D raw data were zero-filled to 256 and 2,048 along F1 and F2 axes and displayed in the magnitude mode (100).

The application of 2D L-COSY on a normal brain correlating different metabolites is shown in Fig. 19. This 2D MRS technique has a great potential for application to neurodegenerative diseases (i.e., AD) for quantification of neurometabolites, particularly the major antioxidant GSH that cannot be definitively quantified by one-dimensional MRS technique.

IV. ALZHEIMER'S DISEASE

Alzheimer's disease (AD), which accounts for around 70% of dementia, is a progressive neurodegenerative disease manifested by cognitive deterioration, progressive impairment of activities of daily living (ADL), and a variety of neuropsychiatric symptoms and behavioral disturbances (50, 51). In normal aging, nerve cells (neurons) in the brain are not lost in large numbers. In AD, however, many nerve cells stop functioning, lose connections with other nerve cells, and die. At first, AD destroys neurons in parts of the brain that control memory, including the hippocampus (a structure deep in the brain that helps encode short-term memories) and related structures (52). As nerve cells in the hippocampus stop working properly, short-term memory fails and a person's ability to do easy and familiar tasks often begins to decline. AD later attacks the cerebral cortex (the outer layer of neurons in the brain), particularly the areas responsible for language and reasoning (53). At this point, AD begins to take away language skills and changes a person's ability to make rational judgments (54). Psychotic symptoms develop in some patients, such as depression, hallucinations, and delu-

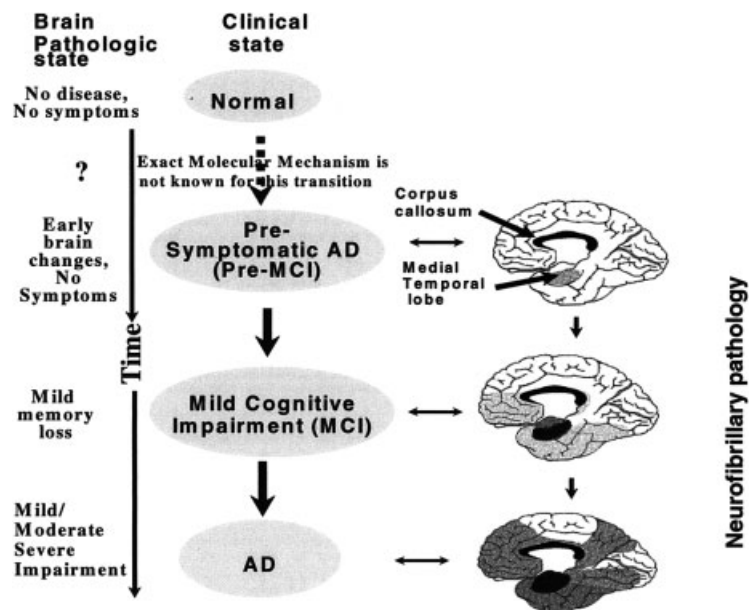


Figure 20 The clinical pathway (normal → pre-MCI → MCI → AD) of AD progression. Postulated sequence of spread of neurofibrillary pathology in AD, showing the medial aspect of the cerebral cortex (101). The depth of the darkness in the brain is in proportion to the density of tangles (102).

sions (55). Eventually other parts of the brain are involved, thereby making the AD brain unresponsive. The fundamental molecular etiology, which leads to neuronal loss resulting in cognitive decline in AD, is unknown. However, there are existing data to support amyloid (56), tau (57), oxidative stress (58), soluble oligomeric A β (59, 60), inflammatory cascade (61, 62), and cholinergic neuronal loss (63) hypotheses in AD. It is not yet known which molecular event initiates the pathocascade of AD (Fig. 20).

Investigators are continuing to use neuroimaging techniques to assess whether it is possible to measure brain neurochemicals to identify people who are at risk of AD even before they develop the symptoms of the disease. Over the past few years, research has expanded our understanding of the potential usefulness of these techniques for research and diagnostic purposes.

MRS in AD

In AD, MRS has demonstrated changes in neurochemistry due to increased oxidative stress (indicated by depletion of brain antioxidant, glutathione) and altered lipid and energy metabolism with the progression of the disease. No studies were identified in the scientific literature that positively correlated these neurochemical changes with clinical findings, established the sensitivity or specificity of MRS in AD, or

compared the diagnostic or prognostic performance of MRS with that of established imaging techniques. MRS has the potential to be used in research studies to monitor the efficacy of drug therapy in AD by measuring alteration of important neurochemicals with time. These neurochemicals are associated with two important biophysical processes (i.e., energy metabolism and lipid metabolism). A brief discussion of these biochemical processes follows.

Energy Metabolism. Brain energy or oxidative metabolism (64) is characterized by (i) high levels of phosphocreatine (PCr) and creatine (Cr); (ii) high levels ATP production; (iii) high activity of creatine kinase (CK); and (iv) high steady-state mitochondrial respiration (Fig. 21A). Because the sine qua non of brain metabolism is a high rate in mitochondrial respiration, the evaluation of energetic balance in the brain under physiological and nonphysiological conditions is important (65).

^{31}P MRS detects distinct signals from the most important metabolites involved in energy transport and storage (i.e., the molecules containing high-energy phosphate bonds). ATP exhibits three peaks in the ^{31}P MRS spectrum corresponding to the three phosphorus atoms (α , β , and γ), and PCr exhibits one peak corresponding to the phosphorus atom (66). In addition, using specific experimental conditions (magnetization transfer), the activity of CK, which

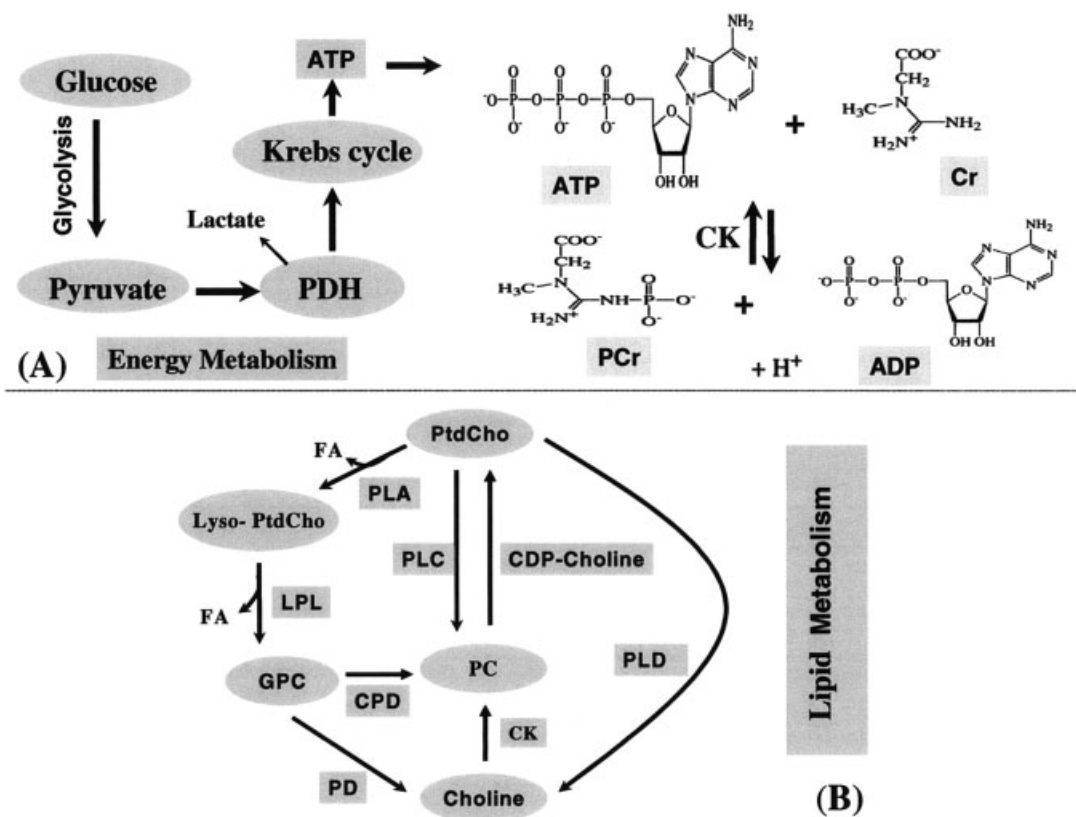


Figure 21 A schematic presentation of energy (A) (64) and lipid metabolism (B) (103). The abbreviations in energy metabolism are as follows: CK, choline kinase; PDH, pyruvate dehydrogenase complex; ATP, adenosine triphosphate; ADP, adenosine diphosphate. Glucose breaks down to pyruvate in the cytosol during glycolysis. (B) The abbreviations in lipid metabolism are as follows: FA, fatty acid; PC, phosphorylcholine; CK, choline kinase; CDP, cytidine diphosphate; PLA, phospholipase A; PLC, phospholipase C; PLD, phospholipase D; LPL, lysophospholipase; CPD, cholinephosphodiesterase; PD, phosphodiesterase.

catalyzes the transfer of the phosphate group of PCr to ADP, can be directly measured (67). PCr is detected together with Cr through its major resonance on a ^1H MRS at 3 ppm, corresponding to N-CH₃ protons (68). In short, the MRS technique is helpful in measuring noninvasively ATP, PCr, and lactate concentrations of the brain under normal and pathological conditions (69–71).

Lipid Metabolism. The brain has a high lipid content, including phospholipids, galactocerebrosides, and gangliosides (72). ^{31}P MRS detects the phosphorus atoms of the head groups in bilayer phospholipids of neuronal membrane. These narrow PDE resonances of the ^{31}P MR spectrum are primarily from GPC and GPE, which are free and mobile in the cytosol and involved in brain lipid metabolism (73) (see Fig. 21B). The PME is mostly composed of signals from phosphoethanolamine (PE) and phosphocholine (PC) (74, 75). Because these resonances consist of over-

lapping signals, the significance of modifications of PME and PDE resonances in pathology is not completely known. Initially it has been proposed that the PME-to-PDE ratio reflects phospholipid turnover (64). PME and PDE corresponds to the molecules involved in the anabolism and catabolism of phospholipids, respectively (76).

^1H MRS in AD

^1H MRS has two great advantages: the proton is the most sensitive stable nucleus, and almost every compound in living tissue contains hydrogen atoms. However, there are technical difficulties. First, the presence of an intense signal from tissue water and, in some cases, from lipids swamp the much smaller signals from metabolites of interest that are present at much lower concentration. Another major problem arises from the narrow chemical shift range of ^1H signals (about 8 ppm). Thus in order to apply in vivo

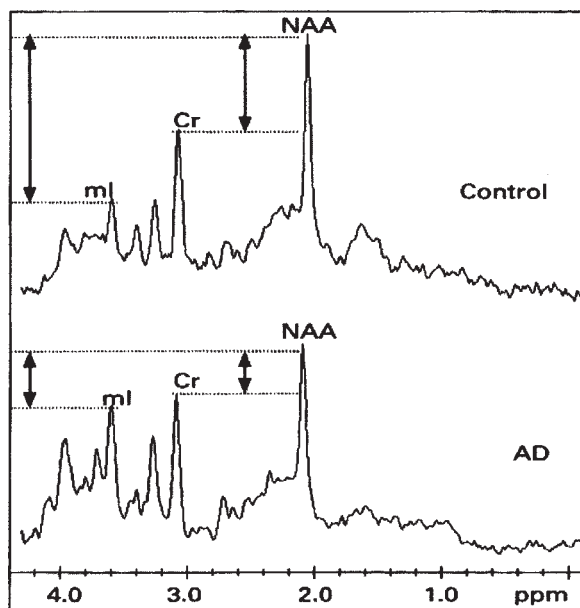


Figure 22 The application of ^1H MRS in AD. Spectra are shown for Control and AD brain in the posterior cingulate region. It is a region of the brain in which there appears to be progressive pathological change throughout the course of AD, and is hence a suitable target for longitudinal studies. NAA/Cr ratio is lower in AD patients compared with Control subjects. In most cases, the ratio NAA/Cr shows good specificity and sensitivity for distinguishing AD patients from Control subjects (104).

^1H MRS successfully, it is necessary to suppress the intense interfering signals (i.e., water and lipids). Moreover, other technical and experimental problems related with the localization, interpretation, and quantification of ^1H MRS spectra should be taken into consideration accurately.

^1H MRS has yielded a growing body of interesting and largely replicable evidence of characteristic metabolite changes in AD (Fig. 22). A consistent finding has been a reduction in NAA levels in AD brains in temporoparietal region (77), temporal lobe (78–80), and parietal lobe (81). Overall, NAA decrease in AD has been shown in at least 18 reports, including in vitro studies showing a correlation with AD pathology (82, 83).

NAA depletion is higher in gray matter compared with white matter in AD. Another striking finding in the literature has been the unforeseen elevation of *mI* levels by about 15% to 20% in the gray matter of patients with AD. Subjects with age-associated memory impairment show no significant increase in *mI* in the temporoparietal region (77), yet one study demonstrated an increased *mI* signal in the posterior cingulate of individuals with mild cognitive impairment (79). No significant *mI* changes have been confirmed

in white matter, but a moderate inverse association between frontal white matter *mI* levels and global mental function has been found (78). The combined NAA/*mI* ratio is robust in discriminating possible AD cases from age-matched control subjects (78, 84). The NAA/*mI* ratio in patients with AD has also been shown to significantly correlate with Mini-Mental State Examination (MMSE) scores and even to significantly predict MMSE change after 12 months (85).

There are intriguing suggestions that ^1H MRS may have a useful role in prognosis of mental function and tracking of disease progression. A noteworthy finding has been the equivalence of in vivo choline estimates between pathologic groups and control subjects.

^{31}P MRS in AD

^{31}P is a naturally occurring nucleus, which has been most extensively used for studying in vivo tissue energetic processes. The spectra are simple as the MR signals are observed only from the relatively mobile compounds, which are in 2–10 mM concentration. Thus, monitoring the relative concentration of various ^{31}P metabolites noninvasively helps to study the biochemistry of diseased and normal states of tissues and to monitor the efficacy of several therapeutic interventions. The spectrum (see Fig. 1B) shows characteristic resonances from β -ATP at -23 ppm and γ -ATP signal at -6.0 ppm. The signal at -7.5 ppm contains contributions from the α -phosphate groups of ATP and adenosine-di phosphate (ADP). The resonances at 0 ppm and 5 ppm are due to PCr and inorganic phosphate (pi), respectively. The chemical shift position of Pi is sensitive to pH and provides a noninvasive indicator of intracellular pH. Besides Pi, ATP, and PCr, signals from phosphomonoesters (PME; 6–8 ppm) and phosphodiester (PDE; 2–4 ppm) are also observed. The metabolic state of cells can thus be studied by monitoring the PME peak.

^{31}P MRS studies of AD have shown abnormalities in the levels of membrane phospholipids and high-energy metabolites that appear dependent on the severity of the illness (22, 23). In normal aging there is a decrease in PMEs accompanied with a concomitant increase in PDE levels, which is different from the profile of biochemical changes in AD (86, 87). Pettegrew and coworkers (22, 86) have reported elevated PME levels in the initial stages of AD compared with age-matched controls. As the illness progresses, PME levels drop. In contrast, PDE levels and high-energy metabolites, such as PCr and Pi, appear to increase as

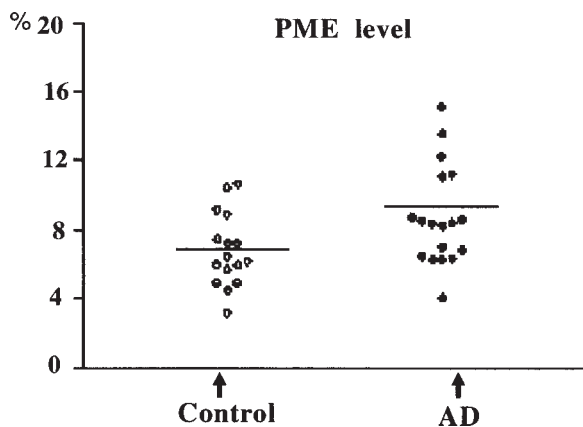


Figure 23 MRS data phosphomonoesters (PME) in AD and Control subjects. Values represent percent areas calculated in terms of the ratio between PME under-peak area to the sum of all under-peak areas within the same spectral curve (105).

the dementia worsens and seem to correlate with the number of senile plaques (22). It has been proposed that the increase in PME reflects early, possibly causative, abnormalities in membrane metabolism, whereas the increase of PDE and PCr reflects neuronal degeneration and death (22, 86).

Abnormalities in the lipid composition (Fig. 23) have been identified in different regions of the brain of AD patients. Anisotropy studies have additionally demonstrated abnormal membrane fluidity in hippocampal synaptosomes (88). Taken together, such findings suggest that aberrations in the synthesis and degradation of membrane phospholipids are metabolic events that occur in AD brains. The intracerebral availability of phospholipid precursors and metabolites, as well as the occurrence of high-energy phosphates, can be estimated by the analysis of the ^{31}P spectral curve within a discrete brain area with the aid of MRS.

It is possible that ^{31}P MRS findings will change during the progression of AD. Longitudinal studies in larger population are needed for the time course of ^{31}P MRS changes in AD. Because ^{31}P MRS yields lower SNR ratio, ^{31}P MRS requires larger voxels, which limits the specificity of the findings from a certain region of the brain. These drawbacks can be overcome using higher-field scanner due to increased SNR at higher field.

Voxel Selection

As the exact location of the postulated biochemical abnormalities is unknown in neurodegenerative disorders, the optimal location for the MRS voxel selection is important. Often voxels are selected on regions

of the brain thought to be involved in a particular psychiatric disease, as determined by other imaging modalities, such as positron emission tomography (PET) or single photon emission computed tomography (SPECT). However, the real possibility exists that the brain abnormality is located in a brain region not sampled by the MRS voxel. As such, the abnormality could be missed altogether. Many studies attempt to sample several locations in a given subject's brain, but in reality, it is only a small percentage of the entire brain volume. Recent studies are using the technique of MRS imaging (MRSI) to sample dozens of voxels at a time, thus reducing this potential for sampling errors. To get high-quality MR spectrum, voxel selection in cerebrospinal fluid (CSF) and near the skull and scalp should be avoided.

Tissue Volume Correction

Most MRS techniques use cubic or rectangular voxels, which do not usually correspond with the curved shapes of the sampled brain regions. As such, a given voxel often samples a combination of cerebrospinal fluid (CSF), gray matter, and white matter. Because CSF has no measurable proton MRS metabolites, the presence of a large fraction of CSF within a voxel will artifactually lower the metabolite concentrations. Furthermore, metabolite concentrations are different in gray matter and white matter (89). New postprocessing techniques have been developed using anatomical images to take these tissue components into account (89). It is also possible to incorporate voxel tissue composition data into the statistical analysis (90) or correct metabolite concentrations (91). To select a voxel in a desired brain region, it is possible to shift the acquisition grid for MRSI studies.

MR Spectra Quantification

Absolute concentration measurements are the ultimate goal of *in vivo* ^1H MRS. Because the signal area is proportional to the amount of nuclei in question, it is in principle possible to quantify metabolite concentration *in vivo*. In practice, however, signal quantification present major technical problems. First, the spectrum itself can be difficult to interpret. It may contain many overlapping peaks (especially if acquired at a short time echo) and due to broad baseline that could come from metabolites with short T_2 . Second, there is inevitable T_1 and T_2 weighting of the resonance peaks, which is dependent on the timing of the localization sequence, as well as signal loss and distortions of coupled peaks. Third, the quality of the localization (i.e., suppression of signals from

outside the VOI) complicates the calculation of the exact volume from which the spectrum was acquired. Finally, a reference signal is required for calibration. This may explain in part the discrepancies between different studies of the same brain region.

The LC-Model (92) is a popular software mostly used in different laboratories for the quantification of the metabolites.

V. LIMITATION OF MRS

At present, ^1H MRS and ^1H MRSI have several limitations. To obtain a good SNR, the experiment duration is still long and can be compromised by patient movement. Furthermore, some brain regions, such as the cerebellum and temporal lobes, that are of pathological interest are difficult to assess due to magnetic field inhomogeneities, which can influence the quality of the spectra. Methodological improvements in localized shimming will allow more reproducible studies from these brain regions in the future.

VI. FUTURE DIRECTION

The ability to perform *in vivo* longitudinal studies from several brain regions and to quantitate metabolite changes provides exciting opportunities for research and as a surrogate tool in assessing putative treatments in many neurodegenerative diseases. Future MRS studies should take advantage of new experimental MRS methods that are relevant to neurodegenerative illness and treatment. A few pioneering studies have examined GABA, the major inhibitory neurotransmitter in the brain (93). Furthermore, Glu is the principal excitatory neurotransmitter in the brain. Using short echo times (TE) techniques, it is possible to measure Glx levels, although until now few studies have examined this peak (90, 91, 94). Because a considerable amount is known about these neurotransmitter systems, detecting GABA or Glu MRS abnormalities in psychiatric patients would be helpful to understand the underlying biochemical defects and to determine optimal treatments.

MRS studies in psychiatric research should also take advantage of new hardware technologies such as high-field MRI machines (3 T and above). Though susceptibility artifacts are considerably increased at high fields, high-order shimming can help smooth out magnetic fields enough to obtain reliable spectroscopic data. Because the signal-to-noise ratio is increased at higher magnetic field strengths, imaging time can be decreased and voxel size can be made smaller. The improvement in available signal afforded

at higher fields also provides for more sophisticated spectral editing techniques, which will allow measurement of some clinically relevant neurotransmitters described previously. The MRSI technique is also valuable because several different brain regions can be studied simultaneously in a single well-positioned slice. This is useful as we do not yet know where the biochemical abnormalities are located in the various neurodegenerative diseases.

Very high-field magnets may also lead to the development of new imaging techniques. For example, animal research suggests a heterogeneous distribution of lithium within the brain parenchyma (95). Ideally, because lithium has a single peak, it should be possible to perform lithium imaging, just as it has been done for sodium. However, such techniques have been hampered by low signal-to-noise ratios caused by small concentrations of lithium within the brain. Higher-field magnets may be able to increase the signal-to-noise such that lithium images can be obtained. Soares and his team have already performed lithium MRS at 3T (96).

Two-dimensional MRS at higher magnetic field strengths (e.g., 7 T) scanner holds strong promise for 2D MRS spectroscopy as it will dramatically increase signal-to-noise ratios and substantially separate the overlapping peaks, which can be quantified without ambiguity.

MRS is a complex and sophisticated neuroimaging technique that allows reliable and reproducible quantification of brain neurochemistry. MRS is already being used to probe the pathophysiology and psychopharmacology of many neurodegenerative disorders, and it is possible that in the future such chemical sampling will generate means of classifying the disorders by neurochemical analysis. Furthermore, MR spectroscopy may permit the analysis of immediate and long-term pharmacotherapeutic interventions and eventually uncover the means to diagnose disorders at a preclinical stage. Clearly, the full clinical potential of neurodegenerative MRS is only beginning to be realized, and it is hoped that further advances in technology will lead to more sensitive and reliable methods of metabolite quantification and localization and perhaps increase the number of compounds—in particular, neurotransmitters that can be detected using spectroscopy.

ACKNOWLEDGMENTS

This article is dedicated to my parents, Mr. Bhardreswar Mandal and Mrs. Kalpana Mandal. I am thankful to Dr. Jay W. Pettegrew (psychiatry) and Dr. Thomas

Albert (radiology, University of California, Los Angeles) for support. Encouragements from Drs. David J. Kupfer (chairman, psychiatry), Oscar L. Lopez (neurology), John P. Williams (chairman, anesthesiology), Fernando E. Boada, Ph.D (radiology), Stephen T. DeKosky (chairman, neurology), Ronald L. Hamilton (neuropathology), Satish Iyenger (chairman, statistics), Brian D. Ross (HMRI, California), and Eliezer Masliah (neuroscience, University of California, San Diego) are appreciated. **Financial support in the form of research grants from the American Health Assistance Foundation, American Parkinson Disease Association, and Alzheimer's Disease Research Center (University of Pittsburgh) is duly acknowledged.** John Wiley & Sons, Inc., is acknowledged for giving permission to reproduce figures. Bradley Mornewick is appreciated for preparing Figure 18. Finally, thanks to Ms. Ratna Mandal for excellent editorial support.

REFERENCES

1. Cady EB, Dawson MJ, Hope PL, Tofts P, de L. Costello A, et al. 1983. Noninvasive investigation of cerebral metabolism in newborn infants by phosphorous nuclear magnetic resonance spectroscopy. *Lancet* 1:1059–1062.
2. Bottomley PA, Hart HR, Edelstein WA. 1984. Anatomy and metabolism of the normal human brain studied by magnetic resonance at 1.5 Tesla. *Radiology* 150:441–446.
3. Hope PL, Cady EB, Tofts P, Hamilton PA, de L. Costello A, et al. 1984. Cerebral energy metabolism studied with phosphorous NMR spectroscopy in normal and birth-asphyxiated infants. *Lancet* 2:366–370.
4. Gillies RJ, Morse DL. 2005. In vivo magnetic resonance spectroscopy in cancer. *Annu Rev Biomed Eng* 7:287–326.
5. Hsu YY, Du AT, Schuff N, Weiner MW. 2001. Magnetic resonance imaging and magnetic resonance spectroscopy in dementias. *J Geriatr Psychiatry Neurol* 14:145–166.
6. Knopman DS, DeKosky ST, Cummings JL, Chui H, Corey-Bloom J, et al. 2001. Practice parameter: diagnosis of dementia (an evidence-based review). Report of the Quality Standards Subcommittee of the American Academy of Neurology. *Neurology* 56:1143–1153.
7. Webb PG, Sailasuta N, Kohler SJ, Raidy T, Moats RA, et al. 1994. Automated single-voxel proton MRS—technical development and multisite verification. *Magn Reson Med* 31:365–373.
8. Wobrock T, Scherk H, Falkai R. 2005. Magnetic resonance spectroscopy in schizophrenia. Possibilities and limitations. *Radiologe* 45:124–130.
9. Ernst R. 1966. Nuclear magnetic double resonance with an incoherent radio-frequency field. *J Chem Phys* 45:3845–3861.
10. Solomon I. 1955. Relaxation processes in a system of two spins. *Phys Rev* 99:559–565.
11. Carr HP, Purcell EM. 1954. Effects of diffusion on free precession in nuclear magnetic resonance experiments. *Phys Rev* 94:630–638.
12. Hahn E, Maxwell D. 1952. Spin-echo measurement of nuclear spin-coupling in molecules. *Phys Rev* 88:1070–1084.
13. Powers R, Gronenborn A, Clore G, Bax A. 1991. Three-dimensional triple-resonance NMR of ¹³C/¹⁵N-enriched proteins using constant time evolution. *J Magn Reson* 94:209–213.
14. Hurd R. 1990. Gradient-enhanced spectroscopy. *J Magn Reson* 87:3422–3428.
15. Sørensen O, Eich G, Levitt M, Bodenhausen G, Ernst R. 1983. Product operator formalism for the description of NMR pulse experiments. *Prog NMR Spectrosc* 16:163–192.
16. Shaka A, Keeler JF, Freeman R. 1983. Evaluation of a new broadband decoupling scheme: WALTZ-16. *J Magn Reson* 53:313–340.
17. Bax A, Freeman R. 1981. Investigation of complex networks of spin-spin coupling by two-dimensional NMR. *J Magn Reson* 44:542–561.
18. Aue W, Bartholdi E, Ernst R. 1976. Two-dimensional spectroscopy. Application to nuclear magnetic resonance. *J Chem Phys* 64:2229–2246.
19. Bain A. 1984. Coherence levels and coherence pathways in NMR. A simple way to design phase cycling procedures. *J Magn Reson* 56:418–427.
20. Bodenhausen G, Kogler H, Ernst R. 1984. Selection of coherence-transfer pathways in NMR pulse experiments. *J Magn Reson* 58:370–388.
21. Mandal PK, Majumdar A. 2004. A comprehensive discussion of HSQC and HMQC pulse sequences. *Concepts Magn Reson Part A* 20A:1–23.
22. Pettegrew JW, Panchalingam K, Moosy J, Martinez J, Rao G, et al. 1988. Correlation of phosphorus-31 magnetic resonance spectroscopy and morphologic findings in Alzheimer's disease. *Arch Neurol* 45:1093–1096.
23. Pettegrew JW, Moosy J, Withers G, McKeag D, Panchalingam K. 1988. ³¹P nuclear magnetic resonance study of the brain in Alzheimer's disease [erratum appears in *J Neuropathol Exp Neurol* 48(1):118–9]. *J Neuropathol Exp Neurol* 47:235–248.
24. Moonen CTW, Sobering G, Vanzijl PCM, Gillen J, Vonkjenlin M, et al. 1992. Proton spectroscopic imaging of human brain. *J Magn Reson* 98:556–575.
25. Byrd SE, Tomita T, Palka PS, Darling CF, Norfray JP, et al. 1996. Magnetic resonance spectroscopy (MRS) in the evaluation of pediatric brain tumors, part II: clinical analysis. *J Natl Med Assoc* 88:717–723.

26. van der Toorn A, Dijkhuizen RM, Tulleken CA, Nicolay K. 1995. T1 and T2 relaxation times of the major 1H-containing metabolites in rat brain after focal ischemia. *NMR Biomed* 8:245–252.
27. Moonen CT, von Kienlin M, van Zijl PC, Cohen J, Gillen J, et al. 1989. Comparison of single-shot localization methods (STEAM and PRESS) for in vivo proton NMR spectroscopy. *NMR Biomed* 2:201–208.
28. Stanley JA. 2002. In vivo magnetic resonance spectroscopy and its application to neuropsychiatric disorders. *Can J Psychiatry* 47:315–326.
29. Pettegrew JW, McClure RJ, Keshavan MS, Minshew NJ, Panchalingam K, et al. 1997. ³¹P magnetic resonance spectroscopy studies of developing brain. In: Keshavan MS, Murray RM, editors. *Neurodevelopment and adult psychopathology*. Cambridge: Cambridge University Press. p 71–92.
30. Pettegrew JW, Panchalingam K, Withers G, McKeag D, Strychor S. 1990. Changes in brain energy and phospholipid metabolism during development and aging in the Fischer 344 rat. *J Neuropathol Exp Neurol* 49:237–249.
31. Kemp GJ. 2000. Non-invasive methods studying for studying brain energy metabolism: what they show and what it means. *Dev Neurosci* 22:418–428.
32. Lei H, Zhu XH, Zhang XL, Ugurbil K, Chen W. 2003. In vivo P-31 magnetic resonance spectroscopy of human brain at 7 T: an initial experience. *Magn Reson Med* 49:199–205.
33. Pettegrew JW, Klunk WE, Panchalingam K, McClure RJ, Stanley JA. 1997. Magnetic resonance spectroscopic changes in Alzheimer's disease. *Ann N Y Acad Sci* 826:282–306.
34. Hetherington HP, Pan JW, Spencer DD. 2002. H-1 and P-31 spectroscopy and bioenergetics in the lateralization of seizures in temporal lobe epilepsy. *J Magn Reson Imaging* 16:477–483.
35. Duncan JS. 1997. Imaging and epilepsy. *Brain* 120:339–377.
36. Gadian DG, Williams SR, Bates TE, Kauppinen RA. 1993. NMR spectroscopy: current status and future possibilities. *Acta Neurochir Suppl (Wien)* 57:1–8.
37. Ruiz-Cabello J, Vuister G, Moonen C, Van Gelderen P, Cohen J, et al. 1992. Gradient-enhanced heteronuclear correlation spectroscopy. Theory and experimental aspects. *J Magn Reson* 100:282–302.
38. Bax A, Pochapsky, SS. 1992. Optimized recording of heteronuclear multidimensional NMR spectra using pulse field gradients. *J Magn Reson* 99:638–643.
39. Frahm J, Bruhn H, Gyngell ML, Merboldt KD, Hanicke W, et al. 1989. Localized proton NMR spectroscopy in different regions of the human brain in vivo. Relaxation times and concentrations of cerebral metabolites. *Magn Reson Med* 11:47–63.
40. Kim H, Thompson RB, Hanstock CC, Allen PS. 2005. Variability of metabolite yield using STEAM or PRESS sequences in vivo at 3.0 T, illustrated with myo-inositol. *Magn Reson Med* 53:760–769.
41. Duyn JH, Gillen J, Sobering G, Vanzijl PCM, Moonen CTW. 1993. Multisection proton MR spectroscopic imaging of the brain. *Radiology* 188:277–282.
42. Brown TR, Kincaid BM, Ugurbil K. 1982. NMR chemical shift imaging in three dimensions. *Proc Natl Acad Sci U S A* 79:3523–3526.
43. Schuff N, Ezekiel F, Gamst AC, Amend DL, Capizzano AA, et al. 2001. Region and tissue differences of metabolites in normally aged brain using multislice 1H magnetic resonance spectroscopic imaging. *Magn Reson Med* 45:899–907.
44. Rothman DL, Petroff OAC, Behar KL, Mattson RH. 1993. Localized H-1-NMR measurements of gamma-aminobutyric-acid in human brain in vivo. *Proc Natl Acad Sci U S A* 90:5662–5666.
45. Petroff OAC, Rothman DL, Behar KL, Mattson RH. 1995. Initial observations on effect of Vigabatrin on in-vivo H-1 spectroscopic measurements of gamma-aminobutyric-acid, glutamate, and glutamine in human brain. *Epilepsia* 36:457–464.
46. Thomas MA, Hetherington HP, Meyerhoff DJ, Twieg DB. 1991. Localization of double quantum filtered 1H MR spectroscopy. *J Magn Reson* 93:485–496.
47. Keltner JR, Wald LL, Frederick BD, Renshaw PF. 1997. In vivo detection of GABA in human brain using a localized double-quantum filter technique. *Magn Reson Med* 37:366–371.
48. Thomas MA, Ryner LN, Mehta MP, Turski PA, Sorenson JA. 1996. Localized 2D J-resolved H-1 MR spectroscopy of human brain tumors in vivo. *J Magn Reson Imaging* 6:453–459.
49. Thomas MA, Yue K, Binesh N, Davanzo P, Kumar A, et al. 2001. Localized two-dimensional shift correlated MR spectroscopy of human brain. *Magn Reson Med* 46:58–67.
50. Cummings JL. 2004. Drug therapy—Alzheimer's disease. *New Engl J Med* 351:56–67.
51. Braak E, Griffing K, Arai K, Braak H. 1999. Neuropathology of Alzheimer's disease: what is new since A. Alzheimer? *Eur Arch Psychiatry Clin Neurosci* 249:14–22.
52. Dixon RM, Bradley KM, Budge MM, Styles P, Smith AD. 2002. Longitudinal quantitative proton magnetic resonance spectroscopy of the hippocampus in Alzheimer's disease. *Brain* 125:2332–2341.
53. Cummings JL. 2000. Cognitive and behavioral heterogeneity in Alzheimer's disease: seeking the neurobiological basis. *Neurobiol Aging* 21:845–861.
54. Killiany RJ, Hyman BT, Gomez-Isla T, Moss MB, Kikinis R, et al. 2002. MRI measures of entorhinal cortex vs hippocampus in preclinical AD. *Neurology* 58:1188–1196.
55. Cummings JL. 2003. Toward a molecular neuropsychiatry of neurodegenerative diseases. *Ann Neurol* 54:147–154.

56. Hardy J, Selkoe DJ. 2002. Medicine—the amyloid hypothesis of Alzheimer's disease: progress and problems on the road to therapeutics. *Science* 297:353–356.
57. Trojanowski JQ, Lee VMY. 2002. The role of tau in Alzheimer's disease. *Med Clin North Am* 86:615–627.
58. Casetta I, Govoni V, Granieri E. 2005. Oxidative stress, antioxidants and neurodegenerative diseases. *Curr Pharm Des* 11:2033–2052.
59. Kaye R, Head E, Thompson JL, McIntire TM, Milton SC, et al. 2003. Common structure of soluble amyloid oligomers implies common mechanism of pathogenesis. *Science* 300:486–489.
60. Mandal PK, Pettegrew JW. 2004. Alzheimer's disease: soluble oligomeric A beta(1–40) peptide in membrane mimic environment from solution NMR and circular dichroism studies. *Neurochem Res* 29:2267–2272.
61. Anderson I, Adinolfi C, Doctrow S, Huffman K, Joy KA, et al. 2001. Oxidative signaling and inflammatory pathways in Alzheimer's disease. *Neuronal Signal Transduction and Alzheimer's Disease* 67:141–149.
62. Cummings JL, Vinters HV, Cole GM, Khachaturian ZS. 1998. Alzheimer's disease—etiologies, pathophysiology, cognitive reserve, and treatment opportunities. *Neurology* 51:S2–17.
63. Francis PT, Palmer AM, Snape M, Wilcock GK. 1999. The cholinergic hypothesis of Alzheimer's disease: a review of progress. *J Neurol Neurosurg Psychiatry* 66:137–147.
64. Vion-Dury J, Meyerhoff DJ, Cozzone PJ, Weiner MW. 1994. What might be the impact on neurology of the analysis of brain metabolism by in vivo magnetic resonance spectroscopy? *J Neurol* 241:354–71.
65. Clarke DD, Lajtha AL, Maker HS. 1989. Intermediary metabolism. In: Seigel G, Agranoff B, Albers RW, Molinoff P, editors. *Basic neurochemistry*. 4th edition. New York: Raven Press. p 541–564.
66. Bottomley PA, Cousins JP, Pendrey DL, Wagle WA, Hardy CJ, et al. 1992. Alzheimer dementia—quantification of energy-metabolism and mobile phosphoesters with P-31 NMR-spectroscopy. *Radiology* 183:695–699.
67. Degani H, Alger JR, Shulman RG, Petroff OA, Prichard JW. 1987. 31P magnetization transfer studies of creatine kinase kinetics in living rabbit brain. *Magn Reson Med* 5:1–12.
68. Miller BL. 1991. A review of chemical issues in 1H NMR spectroscopy: N-acetyl-L-aspartate, creatine and choline. *NMR Biomed* 4:47–52.
69. Chance B. 1989. Metabolic heterogeneity in rapidly metabolizing tissues. *J Appl Cardiol* 4:207–221.
70. Moore CM, Frederick BD, Renshaw PF. 1999. Brain biochemistry using magnetic resonance spectroscopy: relevance to psychiatric illness in the elderly. *J Geriatr Psychiatry Neurol* 12:107–117.
71. Pettegrew JW, Panchalingam K, Stanley JA, McClure RJ. 2002. P-31 and H-1 MRSI studies of psychosis in Alzheimer's disease. *Am J Geriatr Psychiatry* 10:18–19.
72. Agranoff BW. 1989. Lipids. In: Seigel G, Agranoff B, Albers RW, Molinoff P, editors. *Basic neurochemistry*. 4th edition. New York: Raven Press. p 91–107.
73. Merchant TE, Glonek T. 1990. ³¹P NMR of phospholipid glycerol phosphodiester residues. *J Lipid Res* 31:479–486.
74. Brenton DP, Garrod PJ, Krywawych S, Reynolds EO, Bachelard HS, et al. 1985. Phosphoethanolamine is major constituent of phosphomonoester peak detected by ³¹P NMR in newborn brain. *Lancet* 1:115.
75. Petroff OA, Prichard JW, Behar KL, Alger JR, den Hollander JA, et al. 1985. Cerebral intracellular pH by ³¹P nuclear magnetic resonance spectroscopy. *Neurology* 35:781–788.
76. Ruizcabello J, Cohen JS. 1992. Phospholipid metabolites as indicators of cancer cell-function. *NMR Biomed* 5:226–233.
77. Parnetti L, Lowenthal DT, Presciutti O, Pelliccioli GP, Palumbo R, et al. 1996. H-1-MRS, MRI-based hippocampal volumetry, and Tc-99m-HMPAO-SPECT in normal aging, age-associated memory impairment, and probable Alzheimer's disease. *J Am Geriatr Soc* 44:133–138.
78. Parnetti L, Tarducci R, Presciutti O, Lowenthal DT, Pippi M, et al. 1997. Proton magnetic resonance spectroscopy can differentiate Alzheimer's disease from normal aging. *Mech Aging Dev* 97:9–14.
79. Kantarci K, Jack CR, Xu YC, Campeau NG, O'Brien PC, et al. 2000. Regional metabolic patterns in mild cognitive impairment and Alzheimer's disease—a H-1 MRS study. *Neurology* 55:210–217.
80. Jessen F, Block W, Traber F, Keller E, Flacke S, et al. 2000. Proton MR spectroscopy detects a relative decrease of N-acetylaspartate in the medial temporal lobe of patients with AD. *Neurology* 55:684–688.
81. Miller BL, Moats RA, Shonk T, Ernst T, Woolley S, Ross BD. 1993. Alzheimer disease: depiction of increased cerebral myo-inositol with proton MR spectroscopy. *Radiology* 187:433–7.
82. Klunk WE, Xu C, Panchalingam K, McClure RJ, Pettegrew JW. 1996. Quantitative 1H and 31P MRS of PCA extracts of postmortem Alzheimer's disease brain. *Neurobiol Aging* 17:349–57.
83. Mohanakrishnan P, Fowler AH, Vonsattel JP, Husain MM, Jolles PR, et al. 1995. An in vitro 1H nuclear magnetic resonance study of the temporoparietal cortex of Alzheimer brains. *Exp Brain Res* 102:503–10.
84. Shonk TK, Moats RA, Gifford P, Michaelis T, Mandigo JC, et al. 1995. Probable Alzheimer disease: diagnosis with proton MR spectroscopy [see comment]. *Radiology* 195:65–72.

85. Doraiswamy M, Charles C, Krishnan R. 1998. Prediction of cognitive decline in early Alzheimer's disease. *Lancet* 352:1678.
86. Pettegrew JW, Withers G, Panchalingam K, Post JF. 1987. 31P nuclear magnetic resonance (NMR) spectroscopy of brain in aging and Alzheimer's disease. *J Neural Transm* 24(Suppl):261–268.
87. Pettegrew JW, Panchalingam K, Withers G, McKeag D, Strychor S. 1990. Changes in brain energy and phospholipid metabolism during development and aging in the Fischer 344 rat. *J Neuropathol Exp Neurol* 49:237–249.
88. Eckert GP, Cairns NJ, Maras A, Gattaz WF, Muller WE. 2000. Cholesterol modulates the membrane-disordering effects of beta-amyloid peptides in the hippocampus: specific changes in Alzheimer's disease. *Dementia Geriatr Cogn Disord* 11:181–186.
89. McLean MA, Woermann FG, Barker GJ, Duncan JS. 2000. Quantitative analysis of short echo time H-1-MRSI of cerebral gray and white matter. *Magn Reson Med* 44:401–411.
90. Auer DP, Putz B, Kraft E, Lipinski B, Schill J, Holsboer F. 2000. Reduced glutamate in the anterior cingulate cortex in depression: an in vivo proton magnetic resonance spectroscopy study. *Biol Psychiatry* 47:305–313.
91. Villarreal G, Petropoulos H, Hamilton DA, Rowland LM, Horan WP, et al. 2002. Proton magnetic resonance spectroscopy of the hippocampus and occipital white matter in PTSD: preliminary results. *Can J Psychiatry* 47:666–670.
92. Provencher SW. 1993. Estimation of metabolite concentrations from localized in-vivo proton NMR spectra. *Magn Reson Med* 30:672–679.
93. Behar KL, Rothman DL, Petersen KF, Hooten M, Delaney R, et al. 1999. Preliminary evidence of low cortical GABA levels in localized H-1-MR spectra of alcohol-dependent and hepatic encephalopathy patients. *Am J Psychiatry* 156:952–954.
94. Rosenberg DR, MacMaster FP, Keshavan MS, Fitzgerald KD, Stewart CM, et al. 2000. Decrease in caudate glutamatergic concentrations in pediatric obsessive-compulsive disorder patients taking paroxetine. *J Am Acad Child Adolesc Psychiatry* 39:1096–1103.
95. Soares JC, Boada F, Keshavan MS. 2000. Brain lithium measurements with Li-7 magnetic resonance spectroscopy (MRS): a literature review. *Eur Neuropsychopharmacol* 10:151–158.
96. Soares JC, Boada F, Spencer S, Mallinger AG, Dipold CS, et al. 2001. Brain lithium concentrations in bipolar disorder patients: preliminary Li-7 magnetic resonance studies at 3 T. *Biol Psychiatry* 49:437–443.
97. Tkac I, Andersen P, Adriany G, Merkle H, Ugurbil K, et al. 2001. In vivo H-1 NMR spectroscopy of the human brain at 7 T. *Magn Reson Med* 46:451–456.
98. Haase A, Frahm J, Hanicke W, Matthaei D. 1985. 1H NMR chemical shift selective (CHESS) imaging. *Physics Med Biol* 30:341–344.
99. Kim H, Thompson RB, Hanstock CC, Allen PS. 2005. Variability of metabolite yield using STEAM or PRESS sequences in vivo at 3.0 T, illustrated with myo-inositol. *Magn Reson Med* 53:760–769.
100. Thomas MA, Hattori N, Umeda M, Sawada T, Naruse S. 2003. Evaluation of two-dimensional L-COSY and PRESS using a 3 T MRI scanner: from phantoms to human brain in vivo. *NMR Biomed* 16:245–251.
101. DeKosky ST. 2003. Early intervention is the key to successful management of Alzheimer disease. *Alzheimer Dis Assoc Disord* 17:S99–104.
102. Ohm TG, Muller H, Braak H, Bohl J. 1995. Close-meshed prevalence rates of different stages as a tool to uncover the rate of Alzheimer's disease-related neurofibrillary changes. *Neuroscience* 64:209–217.
103. Nitsch RM, Blusztajn JK, Pittas AG, Slack BE, Growdon JH, Wurtman RJ. 1992. Evidence for a membrane defect in Alzheimer disease brain. *Proc Natl Acad Sci U S A* 89:1671–5.
104. Kantarci K, Petersen RC, Boeve BF, Knopman DS, Tang-Wai DF, et al. 2004. H-1 MR spectroscopy in common dementias. *Neurology* 63:1393–1398.
105. Forlenza OV, Wacker P, Nunes PV, Yacubian J, Castro CC, et al. 2005. Reduced phospholipid breakdown in Alzheimer's brains: a P-31 spectroscopy study. *Psychopharmacology* 180:359–365.

BIOGRAPHY



Pravat K. Mandal is a graduate from Indian Institute of Technology, Madras. He did his postdoctoral work at University of California, Davis. At present, Dr. Mandal is an assistant professor (tenure stream) at the Department of Psychiatry, Western Psychiatric Institute Clinic, University of Pittsburgh Medical School. His research interests are Alzheimer's disease, Parkinson's disease, dementia with Lewy body disease, and the role of anesthetics in different neurodegenerative diseases. Dr. Mandal teaches spectroscopy for graduate students.